Nano Research

ISSN 1998-0124 CN 11-5974/O4
https://doi.org/10.26599/NR.2026.94909175

Review Article

Growth, phase engineering, and emerging applications of Pt- and Pd-based transition metal chalcogenides

Xiangyi Ma[1], Lei Zhang[1](✉), Wenshuo Xu[2](✉), Andrew T. S. Wee[1](✉)

[1] Department of Physics, National University of Singapore, 2 Science Drive 3, Singapore 117551, Singapore

[2] Department of Engineering, University of Cambridge, Cambridge CB2 1PZ, UK

Nano Res., **Just Accepted Manuscript** • https://doi.org/10.26599/NR.2026.94909175

https://www.sciopen.com/journal/1998-0124 on Sep. 3, 2026

Just Accepted

Growth, Phase Engineering, and Emerging Applications of Pt- and Pd-Based Transition Metal Chalcogenides

Group-10 transition metal chalcogenides (such as PtS_2, PtS, PdS_2, $PtSe_2$, $PdSe_2$, $PtTe_2$, Pt_2Te_3 and $PdTe_2$) have attracted increasing attention owing to their strong spin-orbit coupling, thickness-dependent band structures, and promising applications in electronics, optoelectronics, spintronics, and energyrelated devices. Recent advances in growth techniques particularly molecular beam epitaxy (MBE), chemical vapor deposition (CVD), and thermal assisted conversion (TAC) have enabled the controllable synthesis of high-quality two-dimensional chalcogenide films. However, a systematic review focusing on the growth of transition metal chalcogenides especially from the perspective of MBE remains lacking. This work is dedicated to filling this gap by providing a comprehensive overview of MBE growth strategies and key parameters as well as other mainstream methods for Group-10 transition metal dichalcogenides (TMDCs) and furthermore, the broader family of Pt- and Pd- based chalcogenides, exploring the growth, phase control, and unique properties of various stoichiometric phases. This review also summarizes their representative physical properties and emerging device applications, aiming to fill the gap in the literature on MBE growth of transition metal chalcogenides and to provide guidance for the controllable synthesis and device integration of high-quality two-dimensional chalcogenide materials.

TABLE OF CONTENTS (TOC)

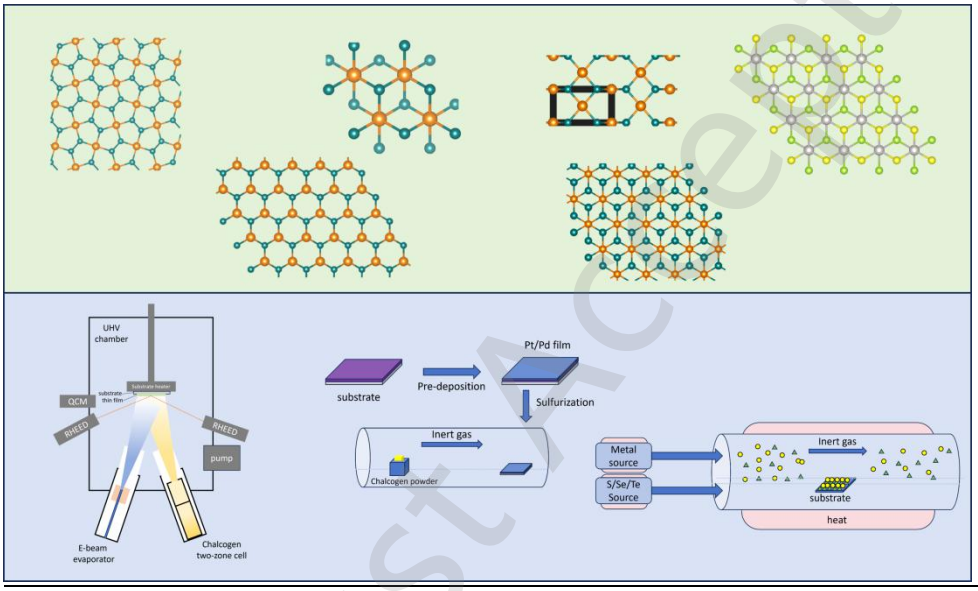

This review provides a comprehensive overview of the growth and phase engineering of Pt- and Pd-based transition metal chalcogenides with particular emphasis on molecular beam epitaxy, , highlighting their tunable physical properties and emerging opportunities in electronic, optoelectronic, spintronic, sensing, and energy-related applications.

Nano Research

Open Access

Review Article/Research Article Please choose on

Growth, phase engineering, and emerging applications of Pt- and Pd-based transition metal chalcogenides

Xiangyi Ma [1], Lei Zhang [1]✉, Wenshuo Xu [2]✉ and Andrew T. S. Wee [1]✉

[1] *Department of Physics, National University of Singapore, 2 Science Drive 3, Singapore 117551, Singapore*
[2] *Department of Engineering, University of Cambridge, Cambridge CB2 1PZ, UK*

Received: 16 June 2026; **Revised:** 20 August 2026; **Accepted:** 3 September 2026

✉Address correspondence to Lei Zhang, zlei@u.nus.edu; Wenshuo Xu, wx256@cam.ac.uk; Andrew T. S. Wee, phyweets@nus.edu.sg

Cite this article: *Nano Research*, 2026, 19, 94909175 https://doi.org/10.26599/NR.2026.94909175

ABSTRACT: Group-10 transition metal chalcogenides (such as PtS_2, PtS, PdS_2, $PtSe_2$, $PdSe_2$, $PtTe_2$, Pt_2Te_3 and $PdTe_2$) have attracted increasing attention owing to their strong spin-orbit coupling, thickness-dependent band structures, and promising applications in electronics, optoelectronics, spintronics, and energyrelated devices. Recent advances in growth techniques particularly molecular beam epitaxy (MBE), chemical vapor deposition (CVD), and thermal assisted conversion (TAC) have enabled the controllable synthesis of high-quality two-dimensional chalcogenide films. However, a systematic review focusing on the growth of transition metal chalcogenides especially from the perspective of MBE remains lacking. This work is dedicated to filling this gap by providing a comprehensive overview of MBE growth strategies and key parameters as well as other mainstream methods for Group-10 transition metal dichalcogenides (TMDCs) and furthermore, the broader family of Pt- and Pd-based chalcogenides, exploring the growth, phase control, and unique properties of various stoichiometric phases. This review also summarizes their representative physical properties and emerging device applications, aiming to fill the gap in the literature on MBE growth of transition metal chalcogenides and to provide guidance for the controllable synthesis and device integration of high-quality two-dimensional chalcogenide materials.

KEYWORDS: 2D materials, group-10 transition metal chalcogenides, molecular beam epitaxy

1 Introduction

Transition metal chalcogenides (TMCs) have emerged as an important class of two-dimensional materials and have attracted extensive attention in condensed matter physics and functional device research. Compared with the conventional group-VI transition metal dichalcogenides (such as MoS_2 and WS_2), chalcogenides formed by group-10 transition metals Pt and Pd, including PtS_2, PtS, PdS_2, $PtSe_2$, $PdSe_2$, $PtTe_2$, Pt_2Te_3 and $PdTe_2$ exhibit richer physical properties in terms of crystal structure, electronic characteristics, and spin-related phenomena. These materials generally possess strong spin-orbit coupling (SOC), pronounced thickness-dependent band structures, and excellent environmental stability, making them promising candidates for applications in two-dimensional electronics, optoelectronics, spintronics, and energy catalysis[1-4].

In the two-dimensional limit, Pt/Pd-based chalcogenides often exhibit unique band structure tunability. Figure 1(a) illustrates the crystal phase structures of representative Pt- and Pd-based transition metal dichalcogenides (TMDCs), including PtS_2, PdS_2, $PtSe_2$, $PdSe_2$, $PtTe_2$, and $PdTe_2$. For example, the electronic structures of materials such as $PtSe_2$ and $PdSe_2$ can evolve continuously from semiconducting to semimetallic states as the layer number increases[5, 6]. Systems such as $PtTe_2$ and $PdTe_2$, owing to their strong SOC and topological band characteristics, have been widely studied as platforms for type-II Dirac semimetals, topological surface states, and two-dimensional superconductivity[7, 8]. In addition, these materials generally exhibit relatively high carrier mobility and anisotropic electronic transport properties, which provide unique opportunities for studying low-dimensional quantum transport and designing next-generation electronic devices.

With the rapid development of material synthesis techniques, the controllable growth of high-quality Pt/Pd-based chalcogenide thin films has made significant progress. At present, molecular beam epitaxy (MBE) and chemical vapor deposition (CVD) are the two major approaches for synthesizing these two-dimensional materials. MBE enables atomic-level control of thickness, flux, and interface structure, making it particularly suitable for obtaining high-quality epitaxial films and investigating intrinsic physical properties. In contrast, CVD is more advantageous for the scalable preparation of large-area films with high uniformity[9, 10]. By tuning parameters such as growth temperature, metal/chalcogen flux ratio, and post-growth treatment conditions, it is possible not only to achieve precise thickness control but also to regulate phase structures and defect distributions, thereby providing valuable experimental routes for studying structure-property relationships.

In terms of functional applications, Pt/Pd-based two-dimensional chalcogenides have demonstrated broad potential across multiple fields. In optoelectronics, these materials can achieve broadband photoresponse ranging from the visible to mid-infrared and even terahertz spectral regions[11, 12]. In spintronics, their strong SOC makes them promising candidates for studying spin Hall effects, spin-orbit torque, and Rashba splitting. In electrocatalysis and gas sensing, catalytic activity and sensing sensitivity can be significantly enhanced through defect engineering, edge modulation, and heterostructure construction[13-15].

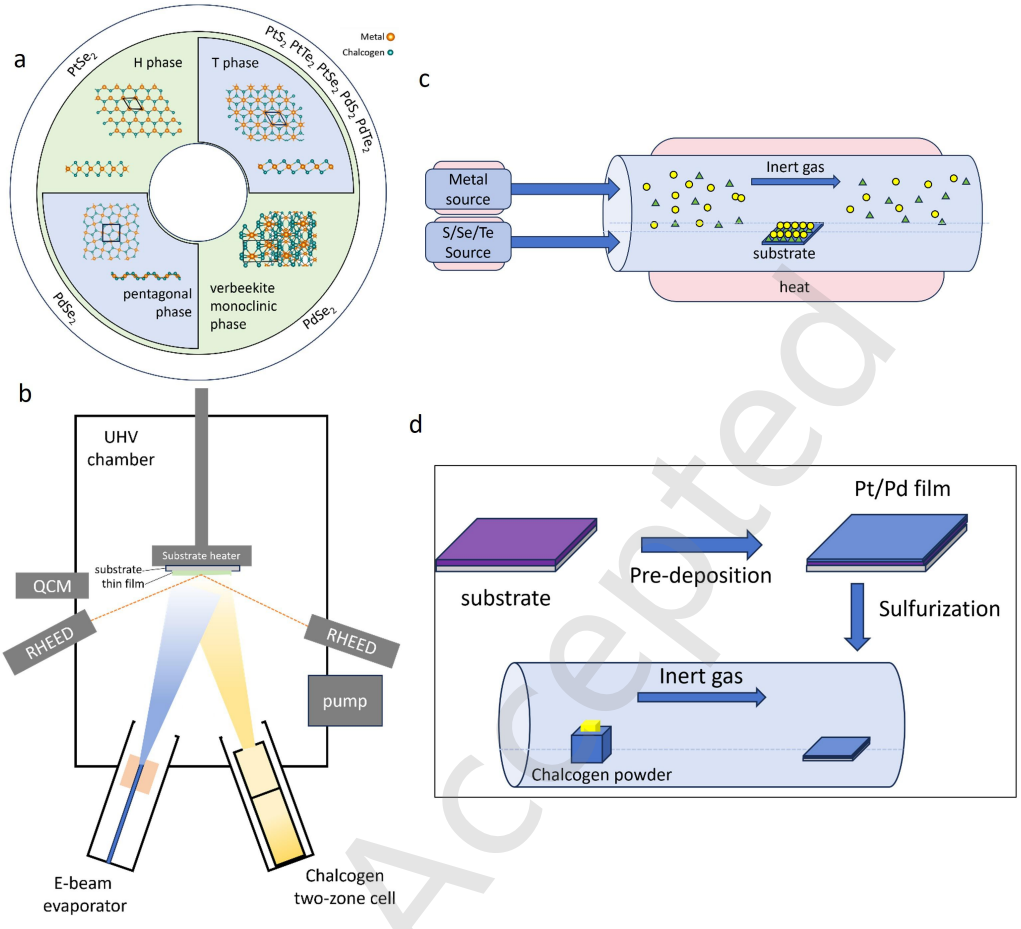

Figure1 (a) Schematic crystal structures of representative Pt- and Pd-based transition metal dichalcogenides (TMDCs), including PtS_2, PdS_2, $PtSe_2$, $PdSe_2$, $PtTe_2$, and $PdTe_2$. (b – d) Schematic illustration of (b) MBE, (c) CVD and (d) TAC growth process for two-dimensional transition metal chalcogenides.

2 Main Synthesis Methods

2.1 Molecular Beam Epitaxy (MBE)

MBE, as illustrated in Figure 1(b), is a physical vapor deposition technique in which high-purity elemental sources are thermally evaporated in ultra-high vacuum (UHV) to form collimated molecular beams that impinge on a heated substrate, enabling layer-by-layer epitaxial growth. Owing to its extremely low background pressure and precise flux control, MBE allows atomic-scale engineering of film thickness, composition, and interface structure, making it particularly suitable for the fabrication of high-quality single-crystalline films and complex heterostructures.

2.2 Chemical Vapor Deposition (CVD)

CVD, as shown in Figure 1(c), is a thin-film growth technique based on chemical reactions of gaseous precursors at the substrate surface. Under elevated temperature or plasma conditions, precursor species undergo decomposition, adsorption, and surface reactions, followed by nucleation and film growth. CVD offers high deposition rates and excellent scalability for large-area uniform films, and is widely used in semiconductor manufacturing and two-dimensional material synthesis.

2.3 Thermally Assisted Conversion (TAC)

TAC, as depicted in Figure 1(d), is a post-growth transformation process in which a pre-deposited precursor film (e.g., metal or compound layer) is converted into the target material through thermal annealing in a reactive atmosphere (such as sulfur, selenium, or oxygen vapor). The process is governed by coupled diffusion and chemical reaction mechanisms, representing a solid-gas phase transformation rather than direct vapor-phase growth. As a result, TAC typically yields polycrystalline films but provides a simple and scalable route for material synthesis.

3 Synthesis and Characterization

3.1 Transition Metal Sulfides

The MBE growth of transition metal sulfides remains technically challenging due to the intrinsic instability of sulfur in UHV environments. The extremely low sublimation temperature of sulfur makes maintaining a stable flux difficult, while its direct use often contaminates both the chamber and electron-beam evaporators[16]. Because large-scale, high-quality sulfide films are difficult to obtain via conventional MBE, CVD serves as the primary synthesis method for PtS_2 and PdS_2.

To circumvent sulfur contamination in MBE, FeS_2 (pyrite) offers a viable alternative source. With a sublimation temperature near 500 °C, FeS_2 thermally decomposes to

release sufficient sulfur flux while leaving the non-volatile Fe atoms behind[17]. Several studies have successfully grown transition metal sulfides using this pyrite-based approach[18-20].

However, well-established reports on the direct MBE growth of PtS_2 or PdS_2 are still lacking. A hybrid route combining MBE and TAC involves depositing ultrathin Pt or Pd films via MBE, followed by an ex-situ or in-situ sulfurization process. Because this approach relies heavily on the initial metal film's uniformity, it is typically paired with in-situ surface probes like reflection high-energy electron diffraction (RHEED) and low-energy electron diffraction (LEED) to monitor structural quality.

3.1.1 Challenges of MBE growth of Pt- and Pd-based Sulfides

In the UHV environment, the epitaxial growth of group-10 transition metal sulfides presents a profound thermodynamic and kinetic paradox. Unlike group-6 TMDCs (e.g., MoS_2 [21]), where strongly negative formation enthalpies firmly anchor volatile sulfur atoms to the high-temperature substrate, group-10 metals are chemically inert due to their nearly filled d-orbitals. The weak Pt-S and Pd-S bonds cannot suppress massive thermal sulfur desorption. Elevating substrate temperatures (> 400 °C) to enhance Pt/Pd adatom mobility simultaneously triggers compound decomposition, whereas lowering the temperature quenches mobility, yielding amorphous or randomly oriented nanocrystals rather than ordered epitaxial films.

This kinetic barrier is uniquely severe for sulfides. While structurally analogous $PtSe_2$ and $PtTe_2$ can be grown via MBE at moderate temperatures (< 300 °C) due to the higher polarizability of diffuse Se and Te electron clouds, the highly localized sulfur anion requires a higher thermal driving force for lattice ordering—directly conflicting with its high vapor pressure. Substituting elemental sulfur with solid precursors like FeS_2[22] stabilizes the incident molecular flux but does not resolve the substrate-side desorption kinetics, as the arriving S_2 molecules still lack the chemical potential to chemisorb onto inert metal surfaces at crystallization temperatures.

Radio-Frequency Plasma-Assisted MBE (RF-PAMBE) offers a promising pathway to bypass this kinetic barrier. Exciting the chalcogen precursor with an RF plasma cracks inert S_2 molecules into highly reactive sulfur radicals (S*)[23]. These radicals possess near-unity sticking coefficients and spontaneously form strong chemisorption bonds with Pt/Pd adatoms without requiring high thermal activation[24]. This enhanced reactivity theoretically decouples the crystallization energy barrier from the substrate temperature, allowing phase-pure PtS_2 and PdS_2 to form where sulfur desorption is naturally suppressed. Alternatively, pre-sulfurizing the substrate with an $(NH_4)_2S_x$ solution creates a uniform S-terminated surface; subsequent deposition of monolayer Pt via e-beam evaporation and UHV annealing successfully yields PtS_2[16].

3.1.2 Synthesis of Pt-based Sulfides with PtS_2 as a Representative System

PtS_2 is an indirect-band-gap layered TMDC. While bulk PtS_2 possesses a band gap near 0.25 eV, quantum confinement in the monolayer limit drastically widens it to 1.6-2.0 eV[25, 26]. Alongside this thickness-dependent tunability and relatively high carrier mobility[27], PtS_2 exhibits exceptional air stability and thermal robustness. It maintains structural integrity and stable vibrational modes across 80-298 K without humidity-induced degradation[28]. Modified CVD and TAC methods have successfully translated these properties to the wafer scale. By precisely regulating the sulfur vapor pressure to suppress the thermodynamically favored PtS phase, continuous PtS_2 films and $PtS_2/PtSe_2$ heterojunctions up to 2 inches in diameter have been fabricated[29, 30]. Because these wafer-scale processes operate at ultralow temperatures (≤ 400 °C), they satisfy back-end-of-line (BEOL) CMOS constraints, allowing direct monolithic integration onto pre-fabricated silicon platforms without damaging underlying circuitry[30]. Figures 2(a)-(d) present representative AFM, Raman spectroscopy, and XPS characterization results of PtS_2 thin films.

TAC techniques typically employ a two-step process to grow PtS_2 and PdS_2. Utilizing H_2S gas rather than elemental sulfur powder enables the direct sulfurization of pre-deposited Pt films into large-area PtS_x films [31-33]. Because the kinetic window is difficult to control, this often leads to nanoparticle formation, non-layered PtS phases, and poor in-plane uniformity. Incorporating variables related to Rayleigh instability such as surface tension, temperature gradients, and mechanical stress into the growth dynamics helps mitigate these issues. Local interfacial anchoring, in particular, successfully yields large-area, single-phase continuous PtS_2 films[34].

Direct CVD growth offers another viable route[35]. Synthesizing PtS_2 on mica substrates using sulfur and $PtCl_2$ precursors reveals a strong temperature-dependent growth behavior: heating the $PtCl_2$ source to 650 °C produces triangular domains with sharp edges, whereas increasing the temperature to 750 °C shifts the morphology toward hexagonal structures[36].

The phase competition during synthesis frequently introduces PtS, a non-layered platinum sulfide characterized by strong three-dimensional covalent networks, as shown in Figure 2(e). This structural divergence renders bulk PtS metallic or weakly semimetallic, lacking the thickness-dependent band-gap modulation of PtS_2. Although its high density of states limits its use in band-gap-engineered transistors, the strong Pt d-orbital contribution ensures excellent electrical conductivity suitable for electrodes and electrocatalysts. During TAC growth, a lower sulfur supply or a thicker initial Pt film thermodynamically drives the formation of PtS over PtS_2 [37, 38], providing a direct mechanism for phase control.

Beyond direct sulfurization, post-growth modification of selenides provides precise chemical tuning. Starting with MBE-grown $PtSe_2$, high-temperature annealing generates selenium vacancies. Exposing this defect-rich lattice to H_2S allows sulfur atoms to selectively occupy the vacancies. Precise adjustment of the H_2S dose and reaction time yields either Janus-type PtSSe structures (S-Pt-Se, as illustrated in Figure 2(f)) or fully sulfurized PtS_2 films[39].

While CVD routes for Pt-based sulfides are well developed, pyrite-assisted MBE provides a cleaner pathway for pristine films. The quantitative control over PtS, PtS_2, and mixed phases demonstrated in CVD suggests that systematically tuning the Pt/S flux ratio in MBE could unlock similarly precise phase engineering in UHV environments.

Although traditionally classified as a van der Waals material, recent electron energy loss spectroscopy (EELS) measurements on PtS_2 reveal substantial out-of-plane orbital hybridization[35]. Figure 2(g) shows the Pt $N_{6,7}$ edge splitting into two sharp peaks, heavily contrasting with the broad, overlapping edges in pure Pt films. This thickness-dependent splitting confirms the presence of interlayer covalent interactions. Thickness-dependent Raman

spectroscopy, shown in Figure 2(h), corroborates this by tracking structural distortions and shifts in the S-Pt bond energy across the inner surface layers.

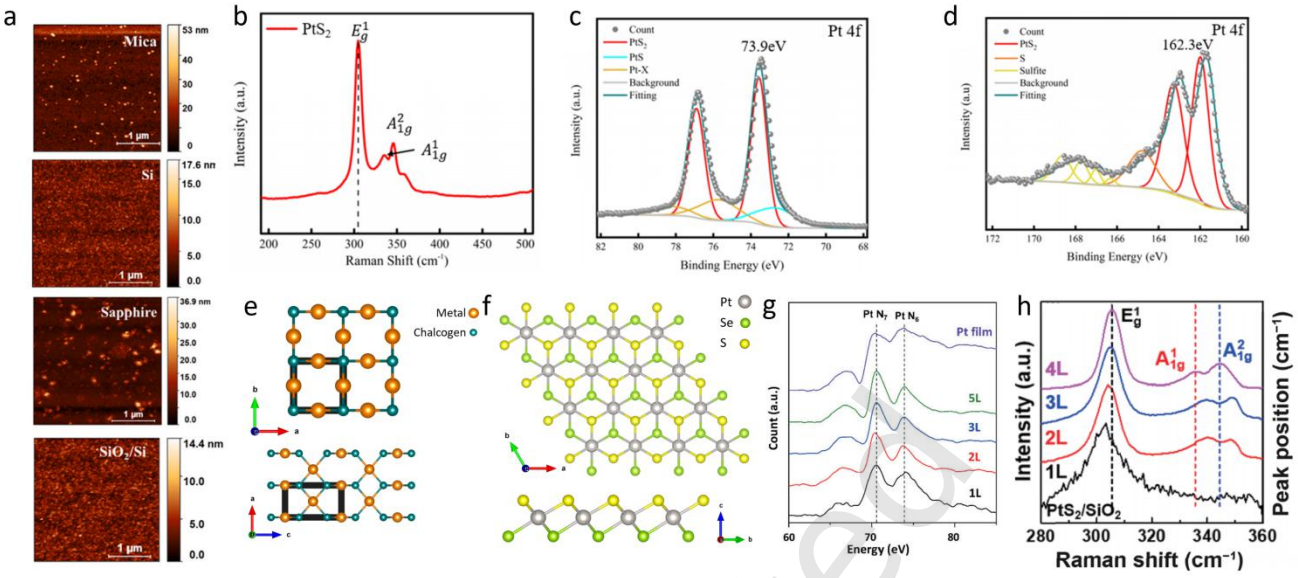

Figure2 (a) AFM image of CVD-grown PtS_2 on different substrate. Reproduced with permission. [4] Copyright 2023, Elsevier. (b – d) (b) Raman spectra and (c, d) XPS characterization of PtS_2 samples obtained by sulfurization of predeposited Pt films at 600 °C for 120 min. Reproduced with permission. [112] Copyright 2024, AIP Publishing. (e – f) Schematic illustrations of the crystal structures of (e) PtS and (f) PtSSe. (g – h) (g) Zoomed-in EELS spectra of the Pt $N_{6,7}$ edge collected from 2D PtS_2 with different layer numbers. (h) Thickness-dependent Raman spectra of transferred PtS_2 ribbons on SiO_2/Si substrates. Reproduced with permission. [42] Copyright 2022, AIP Publishing. Springer Nature.

3.1.3 Synthesis of Pd-based Sulfides with PdS_2 as a Representative System

PdS_2 possesses a stable layered structure defined by pronounced SOC and a tunable band gap[40, 41], making it highly attractive for 2D electronics, spintronics, and catalysis. Recent advancements in scalable deposition have rapidly propelled both its fundamental study and device integration. Few-layer PdS_2 exhibits exceptional environmental durability, maintaining structural integrity and intrinsic Raman modes even after 22 months of ambient exposure, alongside thermal stability across 12-300K[42]. Wafer-scale production relies on coupling electron beam evaporation with atmospheric pressure CVD or TAC to fabricate uniform films up to 2 inches in diameter[43]. Operating at low thermal budgets, these scalable processes comply strictly with the BEOL constraints of silicon CMOS technology, allowing direct monolithic integration of PdS_2 arrays without thermally degrading pre-existing logic circuits[44].

TAC strategies for PdS_2 mirror the two-step processes used for PtS_2. By modulating the activation temperature of sulfur vapors during the reaction, discrete crystalline phases emerge: Pd_4S at 550 °C, PdS at 600 sheshidu, and fully sulfurized PdS_2 at 700 sheshidu[43, 45]. Figures 3(a)-3(c) present the SEM images and corresponding XRD patterns of Pd_4S, PdS, and PdS_2.

Because growth temperatures strictly dictate phase stability and morphology, suppressing intermediate Pd-S compounds is vital for synthesizing pure PdS_2. While MBE growth of PdS_2 remains scarcely reported, the pyrite sulfur source strategy discussed previously presents a promising avenue for yielding epitaxial PdS_2 films, provided the deposition time and thermal windows are tightly optimized to isolate the PdS_2 phase.

TAC growth naturally accommodates compositional engineering. Introducing concurrent sulfur and selenium fluxes yields wafer-scale (2-inch) alloyed $PdS_{2x}Se_{2(1-x)}$ nanofilms with continuously tunable stoichiometry ($0 \leq x \leq 1$). These tunable alloys grow reliably on diverse substrates, including Si/SiO_2, sapphire, soda-lime glass, and mica[46]. Figure 3(d) displays an AFM image of the resulting $PdS_{0.9}Se_{1.1}$ nanofilms.

Combining physical vapor deposition (PVD) with plasma-enhanced CVD (PE-CVD) further optimizes film continuity, producing centimeter-scale few-layer PdS_2 (4.4 to 8.8nm thick) with high chemical purity confirmed by Raman, TEM, and XPS analyses[42]. Temperature-dependent Raman measurements reveal a pronounced polarization anisotropy (Figure 3(e)) and an E_g phonon mode temperature coefficient of approximately 0.0089$cm^{-1}K^{-1}$, reflecting the characteristic interlayer coupling dynamics.

Solution-based synthesis offers an alternative platform for surface functionalization. Preparing PdS_2 nanoparticles via wet chemistry allows for direct capping with ethynylphenylacetylene (EPA) derivatives, where Pd-C≡ conjugated bonds facilitate efficient electronic coupling between the ligand and the PdS_2 core. Compared to control samples capped with 4-ethylphenylthiol (EPT), the EPA-capped nanoparticles exhibit a blue-shifted photoluminescence (PL) peak at 401nm and enhanced emission intensity. Concurrently, XPS shows a >0.2eV reduction in the Pd 3d binding energy, reflecting a substantial redistribution of electronic density (Figures 3(f) and 3(g))[47]. This demonstrates a robust chemical pathway for engineering organic-inorganic hybrid interfaces.

Density functional theory (DFT) computations reinforce the versatility of PdS_2 in heterostructures. The vertical PdS_2/PtS_2 van der Waals stack features a Type-II band alignment with minimal lattice mismatch (<1.1%), which compresses the optical band gap to ~1.5eV and enhances visible-light absorption (Figures 3(h) and 3(i))[48]. The shaded areas in Figure 3(h) mark the excitonic weights of excitons B (blue), G (green), and R (red), projected on the

QP band structure. Structurally, introducing Pd vacancies theoretically induces semimetallicity with a 4 μB magnetic moment, whereas Mo doping triggers a magnetic semiconducting state with red-shifted absorption, expanding utility in spintronics and photovoltaics[49]. Finally, nonadiabatic molecular dynamics (NAMD) simulations of the Cs_2SnBr_6/PdS_2 heterostructure indicate that hydrostatic pressure, coupled with intrinsic SOC, induces Rashba splitting and prolongs carrier lifetimes, providing a theoretical blueprint for perovskite-TMDC hybrid solar cells[50].

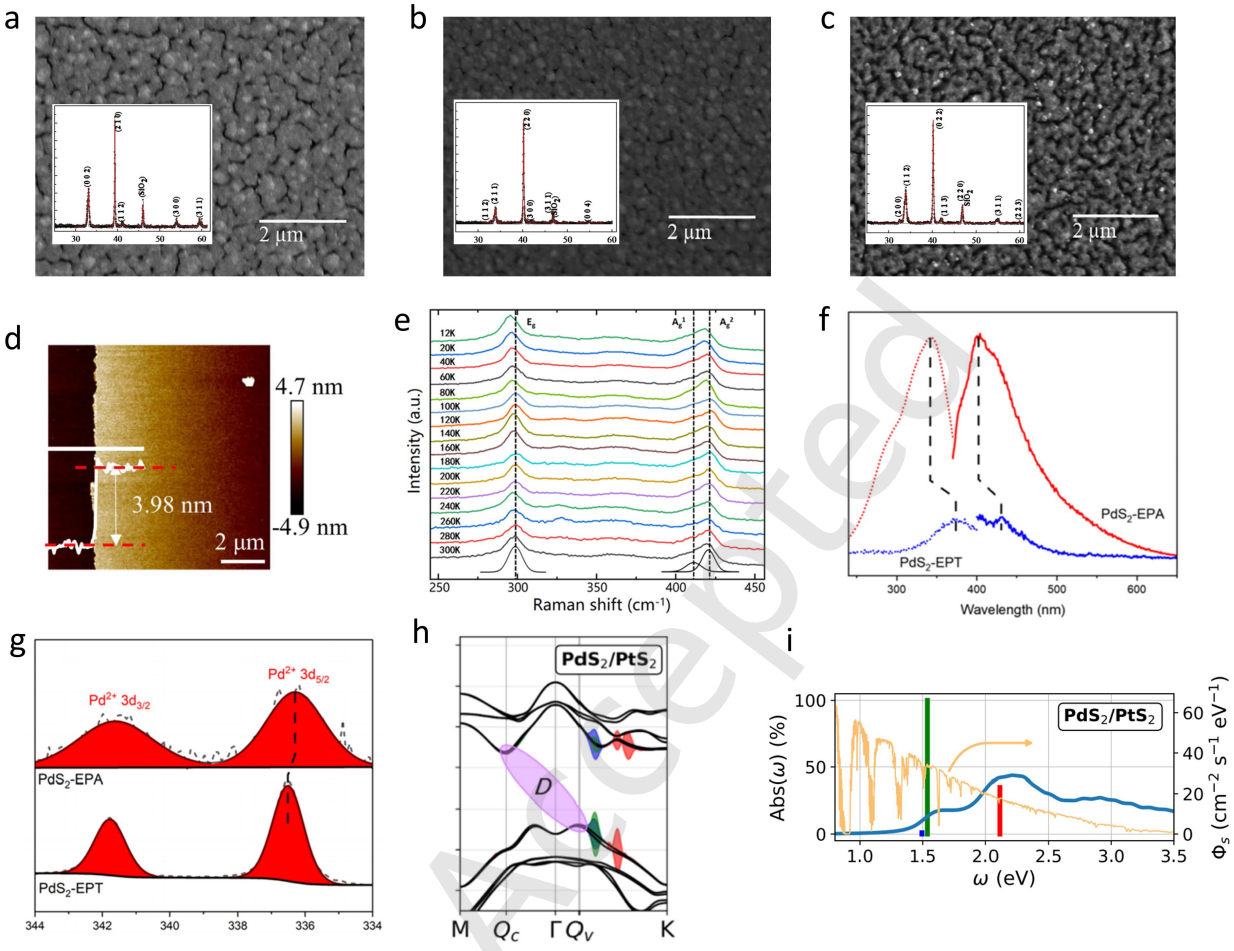

Figure3 (a–c) SEM images and XRD patterns of (a) Pd4S, (b) PdS and (c) PdS_2 films. Reproduced with permission. [6] Copyright 2013, Elsevier. (d) AFM image of $PdS_{0.9}Se_{1.1}$ nanoflakes (NFs). Reproduced with permission. [152] Copyright 2025, Elsevier. (e) Temperature-dependent Raman spectra of few-layer PdS_2. Reproduced with permission. [142] Copyright 2021, American Chemical Society. (f–g) (f) Photoluminescence excitation (dotted lines) and emission (solid lines) spectra of PdS_2-EPA and PdS_2-EPT. (g) XPS spectra of Pd 3d electrons for PdS_2-EPA and PdS_2-EPT. Reproduced with permission. [98] Copyright 2024, American Chemical Society. (h–i) (h) G_0W_0 band structures of the PdS_2/PtS_2 vdW heterostructure (vdWH). The shaded red, green, and blue regions indicate the excitonic weights of the R, G, and B states, respectively. (i) Optical absorbance Abs(ω) of the PdS_2/PtS_2 vdWH. Vertical bars indicate the positions and relative intensities of the R, G, and B excitons. Reproduced with permission. [5] Copyright 2021, American Chemical Society.

3.2 Transition Metal Selenides

Compared with transition metal sulfides, the epitaxial growth of transition metal selenides via MBE is relatively well established. Selenium possesses a higher vapor pressure and more stable evaporation characteristics under UHV conditions, allowing for a more controllable chalcogen flux during growth. As a result, numerous studies have successfully demonstrated the MBE growth of various transition metal selenides, providing systematic insights into their growth mechanisms, structural evolution, and thickness control[51-53].

Transition metal selenides exhibit diverse crystal structures and electronic properties, ranging from semiconducting layered compounds to more complex anisotropic systems. Layered selenides are particularly likely to display strong thickness-dependent electronic structures, attracting considerable interest as two-dimensional materials. Their relatively stable growth conditions under MBE make them important model systems for investigating the epitaxy of chalcogenide thin films.

As representative systems, $PtSe_2$ and $PdSe_2$ illustrate the critical growth parameters for transition metal selenides, including substrate selection, growth temperature, chalcogen-to-metal flux ratios, and post-growth annealing. Examining their synthesis through both MBE and CVD provides a comprehensive understanding of current growth strategies.

3.2.1 Synthesis of Pt-based Selenides with $PtSe_2$ as a Representative System

$PtSe_2$ is a layered transition metal dichalcogenide that combines a van der Waals crystal structure with strong SOC. Its electronic structure can be continuously tuned from semiconducting to semimetallic by varying the number of layers. Compared with conventional group-VI transition metal dichalcogenides such as MoS_2 and WSe_2, ultrathin $PtSe_2$ typically exhibits a wider band gap, relatively high carrier mobility, and excellent environmental stability, making it an attractive material platform for two-

dimensional spintronics, optoelectronics, and quantum transport studies[54, 55]. $PtSe_2$ devices have demonstrated robust air stability, maintaining their optoelectronic and transport performance for over 12 months without the need for complex encapsulation layers, which is a distinct advantage over easily oxidizable narrow-bandgap materials like black phosphorus[56]. The feasibility of its wafer-scale synthesis has also been firmly established through TAC and CVD techniques, yielding highly uniform continuous films up to 4 to 8 inches in diameter via the controlled selenization of pre-deposited Pt layers[57].

$PtSe_2$ exhibits a pronounced thickness-dependent electronic structure. Few-layer $PtSe_2$ (typically $\leq$ 4 layers) behaves as an indirect-band-gap semiconductor, whereas thicker films gradually evolve into a semimetallic state. Figures 4(a) and 4(b) present the second-derivative ARPES spectra of monolayer $PtSe_2$ grown on Pt(111), measured along the high-symmetry K-Γ-M-K directions in the hexagonal Brillouin zone and the corresponding theoretically calculated band structure. The top of the valence band is observed to be at -1.2 eV at the Γ point, while the bottom of the conduction band is above the Fermi level, showing that monolayer $PtSe_2$ is a semiconductor while the theoretical calculation indicates its indirect bandgap[54]. Through such comprehensive momentum-resolved studies combined with theoretical calculations as well as scanning tunnelling spectroscopy (STS) measurements, it is quantified that the indirect band gap decreases dramatically from approximately 2.0±0.1eV in the monolayer to about 0.20±0.1 eV at four layers, with the material crossing the Fermi level to become semimetallic from the fifth layer onward[58]. Realizing this layer-programmable potential imposes stringent demands on synthesis techniques, requiring atomic-level thickness control that dictates the choice of growth methodology.

MBE remains particularly advantageous for fundamental quantum transport and surface-science studies because of its precise control over thickness, stoichiometry, and interface structure. High-quality $PtSe_2$ thin films can be grown by MBE on substrates such as highly oriented pyrolytic graphite (HOPG). Typical growth conditions involve a substrate temperature of approximately 280 sheshidu, which is above the sublimation temperature of Se, ensuring sufficient chalcogen supply during growth. Because Pt and Se possess vastly different vapor pressures, the growth process must be carried out under extreme Se-rich conditions to suppress the formation of thermodynamically favorable Se vacancies. Under these conditions, the film thickness can be precisely controlled by adjusting the flux of the Pt evaporation source[58]. Experimental observations indicate that the crystalline quality of $PtSe_2$ films strongly depends on the Se/Pt flux ratio and post-growth annealing conditions. Maintaining a Se/Pt flux ratio ≥10 is an important process window for achieving high-quality films. A primary limitation of low-temperature MBE, however, is that adatoms often lack sufficient kinetic energy, trapping the as-grown film in a Volmer-Weber (island-like) growth mode. Subsequent annealing in a Se atmosphere at 400 sheshidu for approximately 30 mins provides the necessary activation energy to overcome this kinetic barrier. As shown in Figure 4(c), after annealing, the X-ray diffraction (XRD) peak intensity increases markedly, Raman peaks become sharper with reduced full width at half maximum, and scanning transmission electron microscopy (STEM) images reveal the transition from island-like domains to a continuous layered film, indicating enhanced atomic rearrangement and grain coalescence[59].

Although MBE sets the benchmark for electronic-grade films, its UHV requirements and low throughput necessitate scalable chemical routes. CVD prioritizes scalability over physical vapor deposition but often struggles with morphological control. For example, APCVD has been used to synthesize 1T-phase $PtSe_2$ nanoribbons using $(NH_4)_2PtCl_4$ and Se powder as precursors. When grown on Au foil substrates pre-annealed at 1060 sheshidu, single-crystalline nanoribbons with widths up to ~150μm and thicknesses of approximately 0.9nm can be obtained. By adjusting precursor concentration and reaction time, the morphology and density of the nanostructures can be effectively controlled. AFM and fast Fourier transform (FFT) analyses reveal the presence of well-defined armchair edges and high crystalline quality (Figure 4(d))[60]. Despite achieving excellent crystallinity, this APCVD approach faces two major integration hurdles: the anisotropic growth kinetics intrinsically favor 1D nanoribbons over continuous 2D films, and the extreme thermal budget combined with the reliance on noble metal catalytic substrates precludes direct compatibility with standard CMOS platforms.

Solution-assisted selenization followed by vacuum annealing provides an alternative strategy that connects morphological control with thermodynamic understanding. In this approach, a Pt(111) surface is first selenized in a Na_2Se solution and subsequently subjected to stepwise thermal annealing. This interface-confined reaction offers a direct probe into the thermodynamic phase boundaries of the Pt-Se system. Different surface phases can be obtained depending on the annealing temperature. Annealing at 400 sheshidu leads to the formation of a 2H-phase $PtSe_2$ superstructure, while annealing at 600 sheshidu transforms the surface into a Pt_2Se alloy phase. Further heating to ~750 sheshidu produces a (2×2) defect-ordered structure, and selenium completely desorbs when the temperature exceeds this threshold[61]. This stepwise structural degradation highlights the intrinsic thermal instability of the Pt-Se bond at elevated temperatures.

This sensitivity to thermal treatment acts as both a fundamental processing limitation and a novel engineering opportunity. At elevated temperatures above ~500 sheshidu, few-layer 1T-phase $PtSe_2$ undergoes a thermally driven phase transition due to the loss of Se atoms. As Se desorption changes the stoichiometry from approximately 1:2 to 1:1, the layered $PtSe_2$ structure converts into ultrathin non-layered PtSe crystals within a few minutes, as illustrated in Figure 4(e). In-situ heating experiments combined with TEM and STEM have directly observed this transformation. In UHV annealing at ~500 sheshidu, Se atoms desorb and generate Se vacancies; when their concentration exceeds a critical threshold, $PtSe_2$ undergoes structural reconstruction and converts into a tetragonal non-layered PtSe phase (Figure 4(f))[62].

The electronic properties of the resulting PtSe phase depend strongly on the initial thickness of the parent $PtSe_2$ film, the presence of residual underlying $PtSe_2$, and additional factors such as quantum confinement and strain. Consequently, high-temperature annealing of $PtSe_2$ can yield PtSe films exhibiting either metallic or semiconducting behavior depending on the initial conditions and structural configuration[63]. While severe chalcogen desorption restricts $PtSe_2$ applications in high-temperature environments, this tunable phase transformation expands the functional landscape of Pt-based materials, offering a physical mechanism for developing non-volatile structural

phase-change memory and neuromorphic devices.

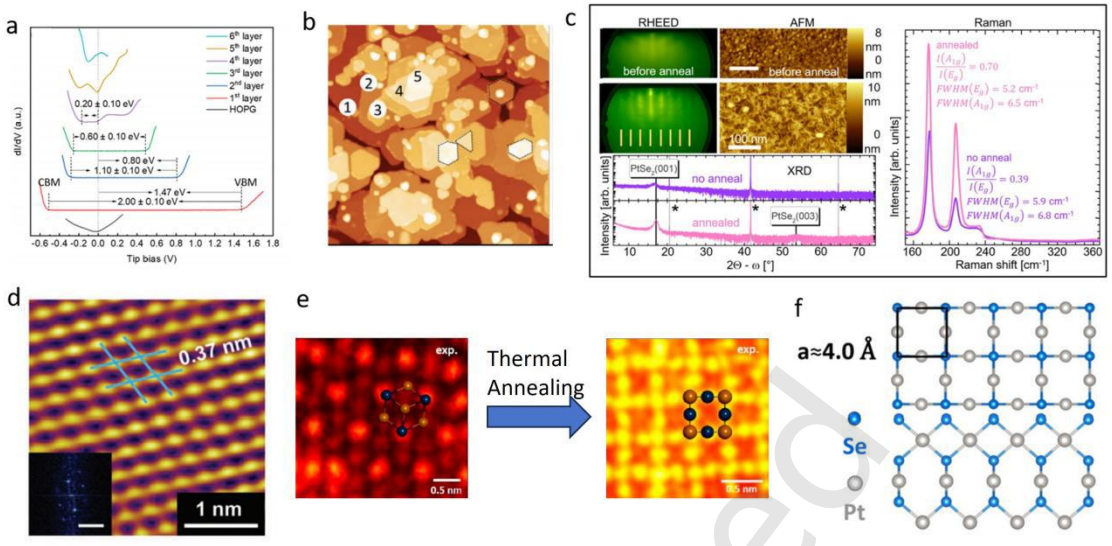

Figure4 (a–b) (a) Second-derivative spectra of the raw ARPES data obtained on the monolayer $PtSe_2$ on Pt(111) along the K–Γ–M–K directions in the hexagonal Brillouin zone. The calculated valence bands are superimposed as green dashed lines. (b) Theoretically calculated band structure and density of states (DOS) of monolayer $PtSe_2$. [114] Copyright 2015, ACS Publications. (c) RHEED, AFM, XRD, and Raman characterization of 10 nm thick $PtSe_2$ layers grown on c-plane sapphire and annealed at 400 °C for 30 min in Se atmosphere after growth. Reproduced with permission. [37] Copyright 2022, IOP Publishing. (d) High-resolution AFM image of $PtSe_2$ ribbons with corresponding FFT analysis. The inset shows the FFT pattern (scale bar: 5 nm−1). Reproduced with permission. [59] Copyright 2023, John Wiley and Sons. (e) ADF-STEM image of $PtSe_2$ and PtSe after phase transition. Reproduced with permission. [91] Copyright 2019, American Chemical Society. (f) Schematic illustration of the top view (top) and side view (bottom) of the crystal structure of PtSe. Reproduced with permission. [154] Copyright 2025, RSC Pub.

3.2.2 Synthesis of Pd-based Selenides with $PdSe_2$ as a Representative System

Systematic investigations of $PdSe_2$ have revealed that this material exhibits remarkable structural stability and tunable electronic properties in the two-dimensional limit. Owing to its puckered crystal structure and strong in-plane anisotropy, $PdSe_2$ has attracted considerable interest as a candidate material for anisotropic electronics, optoelectronic devices, and novel low-dimensional systems. $PdSe_2$ field-effect transistors exhibit exceptional long-term environmental durability, maintaining their intrinsic transport properties and structural integrity without severe degradation even after prolonged exposure to ambient air for several months, vastly outperforming easily oxidizable anisotropic materials like black phosphorus[64, 65]. Highly uniform, wafer-scale 2D $PdSe_2$ layers have been successfully synthesized via the scalable selenization of ultra-thin Pd films, a process accomplished at a remarkably low temperature of 330 sheshidu[66]. Actualizing these device-level promises requires navigating the highly anisotropic growth kinetics and narrow thermodynamic phase window of $PdSe_2$, which dictate the choice between vacuum epitaxy and CVD.

The MBE synthesis of $PdSe_2$ is relatively well developed, providing the atomistic control necessary for probing fundamental surface kinetics. Numerous studies report the successful growth of $PdSe_2$ thin films on a variety of substrates, demonstrating controllable thickness, high crystallinity, and well-defined surface morphology[67-69]. While its UHV requirement restricts high-throughput production, MBE uniquely enables the exploration of structural anisotropy at the quantum limit. Low-dimensional structures derived from $PdSe_2$ have been demonstrated by exploiting the directional surface energies of the puckered lattice. Bottom-up epitaxial growth of $PdSe_2$ nanoribbons has been achieved on top of bilayer $PdSe_2$ islands. These nanoribbons exhibit widths of approximately 5nm and heights of about 7.7Å, extending along the crystallographic b direction with bilayer stacking as the structural unit. This kinetically driven 1D growth mode provides a platform for investigating the electronic and optoelectronic properties of $PdSe_2$ in reduced dimensions. Figure 5(a) shows atomic-resolution and simulated scanning tunnelling microscopy (STM) images (1.0V, 100pA) of the $PdSe_2$ islands.

CVD provides a robust alternative to bypass the scalability bottleneck of MBE, though it faces morphological challenges arising from the same in-plane anisotropy. Few-layer $PdSe_2$ single crystals can be synthesized by LPCVD at approximately 300 sheshidu using $PdCl_2$ and Se powder as precursors. Due to anisotropic growth rates, initial nucleation typically favors isolated, highly faceted domains rather than continuous layers. The resulting films exhibit well-defined layered structures whose thickness can be accurately identified through AFM, second-harmonic generation (SHG), and low-frequency Raman spectroscopy. Figure 5(b) shows AFM images of rectangular-facet $PdSe_2$ crystals with different thicknesses (2L, 5L, and 7L). By balancing the chalcogen supersaturation and mass transport, these discrete nucleation islands can be coaxed into coalescence. Centimeter-scale continuous $PdSe_2$ films with thicknesses ranging from 3 to 15 layers have been successfully grown on sapphire substrates using a three-zone CVD system, providing a scalable route for device fabrication. Representative photographs of $PdSe_2$ samples with different thicknesses are shown in Figure 5(c). Despite this macroscopic success, CVD-grown $PdSe_2$ still suffers from

a high density of grain boundaries generated during island coalescence. These boundaries act as detrimental scattering centers that degrade carrier mobility, necessitating defect-passivation techniques during chemical synthesis.

Solution-assisted synthesis opens a distinct thermodynamic route, enabling the stabilization of unique stoichiometries that resist conventional high-temperature CVD. Additional Pd-Se phases can be derived through thermal transformation. When using a drop-casting method with allylpalladium(II) chloride dimer as the precursor, either $PdSe_2$ or Pd_2Se_3 can be obtained by changing the solution concentration[70]. This concentration-dependent phase selection reveals a sensitive competition between nucleation pathways at the liquid-solid interface. Figure 5(d) shows the ADF-STEM image of $PdSe_2$ and Pd_2Se_3 nanoflakes growing on graphene with the precursor solution concentration of 0.1 millimolar. Pd_2Se_3 adopts an orthorhombic structure with lattice constants a = 5.95Å and b = 6.12Å, with each unit cell containing four Pd atoms and six Se atoms[71]. The resulting monolayer forms a lace-like planar structure, while the side view reveals a staggered pentagonal configuration. Various types of structural defects have been observed in monolayer Pd_2Se_3, including point vacancies, one-dimensional wave-like defects, grain boundaries with 90° or 45° misorientation, and defect-ring complexes. While these intricate defect landscapes present a hurdle for reproducible macroscopic electronic transport, they simultaneously provide a fertile playground for single-atom catalysis and localized quantum emission. These diverse defect behaviors differ significantly from those observed in structurally rigid group-VI TMDCs, underscoring both the synthetic challenges and the rich structural physics inherent to the Pd-Se system.

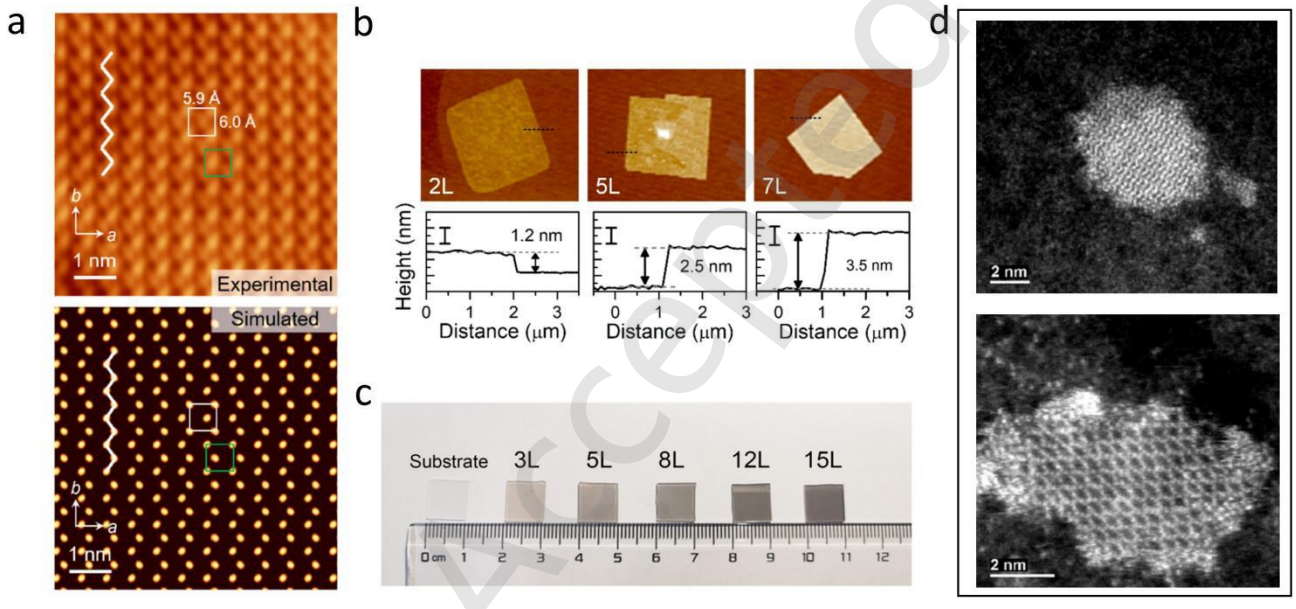

Figure5 (a) Atomic-resolution (top) and simulated STM images (bottom) of $PdSe_2$ islands (1.0 V, 100 pA). Reproduced with permission. [53] Copyright 2018, Springer Nature. (b) AFM images of few-layer $PdSe_2$ with rectangular facets (2L, 5L, and 7L). Reproduced with permission. [70] Copyright 2020, American Chemical Society. (c) Photographs of $PdSe_2$ samples with different numbers of layers. Reproduced with permission. [118] Copyright 2022, Springer Nature. (d) ADF-STEM images of $PdSe_2$ (top) nanoflake and Pd_2Se_3 (bottom) nanoflakes with 0.1 mM precursor growth on graphene. Reproduced with permission. [102] Copyright 2020, American Chemical Society.

3.3 Transition Metal Tellurides

The growth behavior of Pt- and Pd-based tellurides reveals complex epitaxial mechanisms and structural characteristics. The MBE growth of transition metal tellurides has matured significantly in recent years. Owing to the favorable vapor pressure and controllable flux of tellurium under UHV conditions, a wide range of transition metal tellurides can now be synthesized using MBE. Through careful control of growth parameters—including substrate temperature, chalcogen-to-metal flux ratio, and post-growth annealing conditions, it is possible to realize phase-selective growth and the formation of mixed-phase compounds. These capabilities provide a versatile platform for studying the structural and electronic properties of telluride-based two-dimensional materials.

Pt- and Pd-based tellurides stand out among transition metal tellurides due to their distinctive crystal structures, strong SOC, and diverse electronic properties. Many of these compounds exhibit metallic or semimetallic characteristics and have been proposed as candidate materials for topological phases, spintronic devices, and catalysis-related applications. Several Pt- and Pd-based tellurides possess layered structures that can be thinned down to the few-layer or monolayer limit, enabling the exploration of thickness-dependent electronic phenomena.

3.3.1 Synthesis of Pt-based Tellurides with $PtTe_2$ as a Representative System

Synthesizing Pt-based tellurides presents a unique thermodynamic challenge: balancing the extreme sensitivity of their topological states with scalable manufacturing. $PtTe_2$ possesses a typical layered crystal structure, and its electronic and spin-related properties are highly sensitive to both layer number and crystal symmetry. Consequently, this material exhibits rich physical phenomena and promising prospects for device applications. $PtTe_2$ maintains its intrinsic crystalline phase and stable optoelectronic properties after prolonged atmospheric exposure[72], demonstrating remarkable environmental and chemical stability for practical integration. The feasibility of its scalable wafer-level manufacturing has been robustly demonstrated. Highly uniform, continuous $PtTe_2$ films and patterned arrays up to 2 inches in diameter have been

successfully synthesized through a straightforward, one-step tellurization of pre-deposited Pt films[73]. $PtTe_2$ crystallizes in a trigonal 1T phase, distinguishing it from commonly studied hexagonal TMDCs. In this structure, Pt atoms occupy the center of a Te-Pt-Te sandwich layer, forming an environment with strong SOC while preserving inversion symmetry. As illustrated in Figure 6(a), DFT calculations indicate that monolayer (1L) $PtTe_2$ behaves as an indirect-band-gap semiconductor with a band gap of approximately 1.2 eV. Starting from the bilayer (2L), hybridization between$Te\ p_z$ orbitals across the van der Waals gap becomes increasingly significant, leading to a gradual evolution of the electronic structure toward a semimetallic state[74-76]. This layer-dependent electronic transition reveals an unusual band-structure evolution and provides new opportunities for controlling electronic transport and spin polarization through thickness engineering. This abrupt semiconductor-to-semimetal transition acts as a double-edged sword: while it offers unprecedented tunability for layer-programmable spintronics, it simultaneously demands absolute, atomic-precision thickness control during synthesis to prevent spatial phase fluctuations in macroscopic devices.

Rigorously probing these thickness-dependent topological transitions relies heavily on MBE. While conventional CVD techniques prioritize throughput, they invariably introduce high densities of grain boundaries and point defects that scatter topologically protected carriers. MBE offers improved control over film crystallinity and surface morphology, thereby mitigating issues such as surface roughness and high grain-boundary density that often arise in CVD-grown films. By adjusting the growth temperature window, different Pt-Te phases can be obtained, as schematically illustrated in Figure 6(b). The effective Te:Pt ratio during growth varies with temperature. Under typical growth conditions, the substrate temperature is maintained at approximately 280sheshidu-300sheshidu to obtain large-area, high-quality bilayer $PtTe_2$ films. At temperatures exceeding 300sheshidu, Te atoms may partially dissociate or desorb, altering the Te:Pt ratio and potentially introducing Te vacancies or inducing phase transformations within the Pt-Te system[74]. This narrow thermal window underscores a fundamental growth bottleneck: maintaining pristine 1T-$PtTe_2$ stoichiometry strictly limits the thermal budget, restricting the kinetic energy available for adatom mobility and defect self-healing.

Maintaining a high Te:Pt flux ratio during MBE ensures a complete reaction between Pt and Te. The ability to grow $PtTe_2$ films with well-controlled thickness enables systematic investigations of their thickness-dependent electronic properties. ARPES measurements for films of different thicknesses are shown in Figure 6(c). In the low-energy region, the 2 monolayer (2 ML) film exhibits a purely two-dimensional metallic band dispersion without a clear Dirac-cone feature. In the 3 ML film, two V-shaped pockets emerge near the Γ point (indicated by red arrows), suggesting the onset of Dirac-state formation. For thicker films (4 ML and 6 ML), these V-shaped pockets shift downward in energy and merge with hole-like pockets at higher binding energies, resulting in the three-dimensional type-II Dirac fermion dispersion characteristic of bulk $PtTe_2$. In the high-energy region, the 2 ML film exhibits two separated bands with M-shaped and W-shaped dispersions, with a gap between them. As the thickness increases to 3 ML, the two bands approach each other and the gap decreases. For 4 ML and 6 ML films, the two bands fully merge to form a Dirac-cone structure corresponding to topological surface states. These observations demonstrate that the electronic structure of $PtTe_2$ evolves significantly with thickness, completing the transition from a two-dimensional metal to a three-dimensional type-II Dirac semimetal, a class of quantum materials featuring strongly tilted Dirac cones, where Lorentz invariance is broken at the intersection of electron and hole pockets, at a thickness of approximately 4-6 ML[77]. This compelling ARPES evidence confirms that MBE-grown $PtTe_2$ can cleanly host topological surface states; nevertheless, maintaining this exact layer thickness over technologically relevant length scales remains a prohibitive challenge for current MBE technology.

Recent advances have actively harnessed thermal instability kinetics for dynamic phase engineering. Methods such as high-temperature annealing above 300sheshidu, re-tellurization, or additional Pt deposition can trigger phase transitions within Pt-Te compounds[78, 79]. Figure 6(d) illustrates the phase transformation between $PtTe_2$ and $PtTe_2$/PtTe heterostructures achieved through high-temperature annealing followed by re-tellurization, while Figure 6(e) presents a STEM image of the resulting $PtTe_2$/PtTe heterostructure. The precise control over such crystalline interfaces provides a powerful platform for tuning the Rashba SOC, a defining feature of heavy transition metal chalcogenides. A global Rashba effect emerges in these heterostructures due to the explicit breaking of macroscopic structural inversion symmetry at the $PtTe_2$/PtTe boundary. This enables the controllable manipulation of macroscopic spin-split bands through the reversible phase conversion between the symmetric and asymmetric structures[80]. The influence of SOC in these materials extends far beyond interfacial symmetry breaking. Recent compelling studies reveal that even in pristine, globally centrosymmetric bulk $PtTe_2$ and $PtSe_2$, where the global Rashba parameter is ostensibly zero, a pronounced local Rashba effect dominates the electronic structure. Because the local atomic site symmetry lacks inversion symmetry, strong spatially segregated spin polarizations are induced. These localized spin states perfectly compensate each other over the unit cell to preserve global symmetry, yet they can be individually probed or selectively addressed for localized spintronic operations[81]. The coexistence and tunability of both global (heterostructure-driven) and local (lattice-driven) Rashba effects establish Pt- and Pd-based chalcogenides as exceptionally rich playgrounds for advanced spin manipulation. While these in-situ phase transformations offer an elegant mechanism for creating monolithic topological-to-trivial junctions and actively modulating these Rashba states, accurately terminating the tellurium desorption process at the exact stoichiometric boundary of PtTe poses a severe challenge for scalable reproducibility.

TAC has emerged as a highly viable, scalable route to overcome the throughput limitations of MBE and translate $PtTe_2$ into industrial applications. The TAC synthesis of $PtTe_2$ has been extensively studied and is particularly suitable for the rapid preparation of large-area thin films. A Pt thin film acts as the precursor and subsequently converts into $PtTe_2$ through a tellurization reaction governed by a solid-state diffusion mechanism. By reducing the tellurization temperature to approximately 400sheshidu, high-quality $PtTe_2$ films can be obtained in a controllable manner. As shown in Figure 6(f), the thickness and continuity of the resulting $PtTe_2$ films can be tuned by adjusting the coverage of the Pt precursor layer[72]. This growth window has been widely adopted for the fabrication and characterization of device-grade $PtTe_2$ films[82, 83]. By strictly regulating the Te

precursor flux, a previously elusive PtTe phase can be isolated, which can then be converted into $PtTe_2$ through high-temperature tellurization[84]. A critical side effect of this solid-state conversion is the massive volume expansion accompanying tellurization, which typically induces severe compressive strain and micro-cracking within the continuous film.

Mitigating this mechanical degradation requires precise pre-patterning and engineering of the initial metal precursor. Highly oriented single-crystalline 1T-$PtTe_2$ films can be obtained by tellurizing engineered Pt(111) thin films. Tuning the Volmer-Weber epitaxial growth mode of the initial Pt film reserves sufficient lateral expansion space for the formation of $PtTe_2$ during tellurization. This strategy effectively relieves strain accumulation during the phase transformation process and suppresses lattice distortion and film cracking[85]. While TAC currently represents one of the most promising routes toward wafer-scale CMOS integration, bridging the mobility gap between these conversion-grown polycrystalline films and pristine MBE single crystals remains the defining material science challenge for the next generation of $PtTe_2$ platforms.

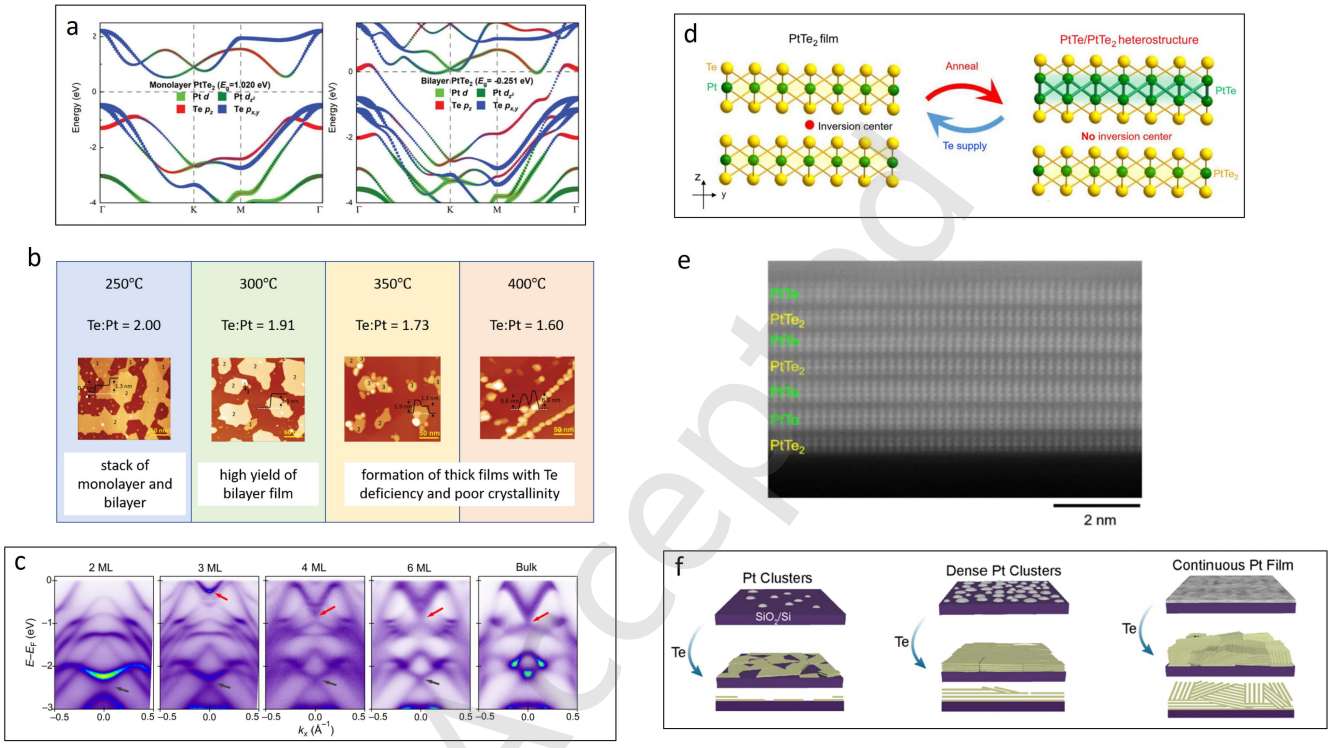

Figure6 (a–b) (a) The HSE06 band structures of monolayer (left, semiconductive) and bilayer (right, semimetallic) $PtTe_2$. (b) STM images of $PtTe_2$ grown at different growth temperatures. Reproduced with permission. [137] Copyright 2022, RSC Pub. (c) Measured ARPES spectra of $PtTe_2$ films with different thicknesses (2–6 ML) and bulk crystals along the Γ–K direction. Reproduced with permission. [17] Copyright 2019, Elsevier. (d–e) (d) Crystal structures of $PtTe_2$ and PtTe/$PtTe_2$ heterostructure (side view). (e) STEM image of the PtTe/$PtTe_2$ heterostructure. Reproduced with permission. [24] Copyright 2025, Springer Nature. (f) Schematic illustration of $PtTe_2$ film growth via tellurization of different types of Pt precursors. Reproduced with permission. [113] Copyright 2020, American Chemical Society.

3.3.2 Synthesis of Pd-based Tellurides with $PdTe_2$ as a Representative System

$PdTe_2$ exhibits a pronounced thickness-dependent electronic structure governed by strong SOC. Its exceptional long-term environmental stability resolves a major degradation bottleneck that typically plagues topological semimetals. Experimental evaluations have demonstrated that the intrinsic transport properties and quantum states of macro-scale, ultrathin $PdTe_2$ films remain fundamentally intact even after continuous ambient air exposure for up to 20 months[86]. Scalable wafer-level manufacturing has been robustly validated; by utilizing advanced growth techniques such as self-stitched epitaxy (SSE), highly uniform and continuous $PdTe_2$ layers up to the inch-level scale have been successfully synthesized at a remarkably low thermal budget of approximately 300sheshidu[87]. In the few-layer limit, $PdTe_2$ shows a tunable band gap that gradually decreases with increasing thickness. When the thickness falls below approximately 6 ML, the material retains a finite band gap, whereas beyond this critical thickness it evolves into a semimetallic state. This transition reflects the gradual evolution from a two-dimensional electronic system toward quasi-bulk behavior[88-91]. Such layer-dependent electronic characteristics provide an important material basis for programmable band-structure engineering and low-dimensional topological state manipulation. Mapping this layer-dependent physics into practical device arrays necessitates advanced growth techniques capable of bridging the gap between atomic-scale epitaxy and macroscopic uniformity.

MBE and direct substrate tellurization dominate the probing of fundamental quantum limits, though their success relies heavily on substrate-adatom interactions. The MBE growth of $PdTe_2$ is relatively well established, enabling epitaxial growth on various substrates with controlled thickness and morphology. Typical growth temperatures sit around 250sheshidu[92], although few-layer $PdTe_2$ films can form at lower temperatures under carefully controlled conditions[93]. Figures 7(a) and 7(b) show the STM images of $PdTe_2$ films with different surface coverages, illustrating the evolution of island morphology during the growth process. This island-like Volmer-Weber growth mode highlights a persistent kinetic challenge: the inherently weak van der Waals interaction with inert substrates often leads to delayed droplet coalescence, generating grain boundaries that scatter topologically protected carriers.

Direct tellurization of single-crystal Pd surfaces circumvents this kinetic barrier and enforces continuous 2D growth by utilizing the substrate as a reactive template rather than a passive support. Large-area, high-quality monolayer Pd-Te structures emerge through direct tellurization of Pd(111) surfaces under UHV conditions. In such epitaxial systems, annealing at approximately 470sheshidu leads to the formation of a well-ordered monolayer $PdTe_2$ structure. Characterization using STM, XPS, and LEED confirms the formation of a hexagonal lattice with an atomic spacing of approximately 4.7Å and excellent thermal stability, showing no decomposition even after annealing at 470sheshidu[94]. Figure 7(c) presents a representative STM image of $PdTe_2$, while Figure 7(d) shows atomic-resolution STM images of the lattice structure.

This strong substrate-epitaxy coupling forcefully stabilizes metastable polymorphs that defy bulk thermodynamic rules. The direct tellurization method can produce metastable pentagonal monolayer $PdTe_2$. Comprehensive characterization using STM, XPS, LEED, high-resolution electron energy loss spectroscopy (HREELS), and ARPES reveals that this structure exhibits a low-symmetry atomic arrangement consisting of one-dimensional zigzag chains. The unit cell dimensions measure approximately 6.2 × 6.2Å, corresponding to a $(\sqrt{5} \times \sqrt{5})R26.6°$ supercell relative to the underlying Pd(100) substrate lattice. The metastable structure is stabilized specifically through lattice matching with the substrate. Figures 7(e)-(h) show the schematic lattice structures and atomic-resolution STM images of monolayer hexagonal and pentagonal $PdTe_2$. DFT calculations and experimental measurements indicate that this phase behaves as an indirect-band-gap semiconductor with a band gap of approximately 1.05eV. HREELS measurements reveal phonon modes at 23meV and 26meV, and the material remains stable even after exposure to ambient conditions. While utilizing substrate symmetry to synthesize anisotropic pentagonal phases advances fundamental materials science, the inherently strong interfacial bonding severely impedes mechanical exfoliation. Transferring these metastable electronic phases into arbitrary van der Waals heterostructures or silicon-based logic architectures remains a significant unsolved challenge.

Industrial efforts have expanded toward top-down chemical transformations and physical vapor deposition to address the scalability limitations and transfer constraints of UHV epitaxy. $PdTe_2$ thin films can be fabricated using industrial deposition techniques such as direct-current magnetron co-sputtering, enabling scalable synthesis and heterostructure device fabrication[95]. While sputtering resolves the macroscopic area problem, the resulting polycrystalline nature inevitably degrades quantum transport, requiring extreme thermodynamic routes to access high-quality non-layered phases. Related Pd-Te compounds such as PdTe have also attracted interest due to their superconducting properties. Superconductivity in PdTe was first reported in 1953[96]. Bulk PdTe crystals can be synthesized by high-temperature vacuum melting methods, producing air-stable crystals whose XRD patterns confirm a single-phase NiAs-type hexagonal structure, as illustrated in Figures 7(i) and 7(j)[97].

$PdTe_2$ serves as a unique parent matrix for electrochemically driven dimensionality reduction, connecting the pristine quality of bulk melting with the requirements for 2D geometries. It provides a robust platform for in-situ electrochemical phase transformations from layered to non-layered phases. In device configurations, $PdTe_2$ undergoes electrochemically driven stoichiometric conversion in molten electrolytes under an applied bias. During this process, Pd^{4+} intercalation and chemical transformation lead to the formation of ultrathin PdTe sheets in the two-dimensional limit. These resulting structures exhibit anisotropic upper critical fields and clear two-dimensional superconducting characteristics[98]. This electrochemical stripping effectively bypasses the thermodynamic impossibility of growing non-layered 2D PdTe from the bottom up. Precise spatial and temporal control of the intercalation kinetics forms a major bottleneck for future device engineering; over-driving the electrochemical bias inevitably triggers irreversible structural collapse, currently limiting the reproducible yield for scalable topological superconducting junctions.

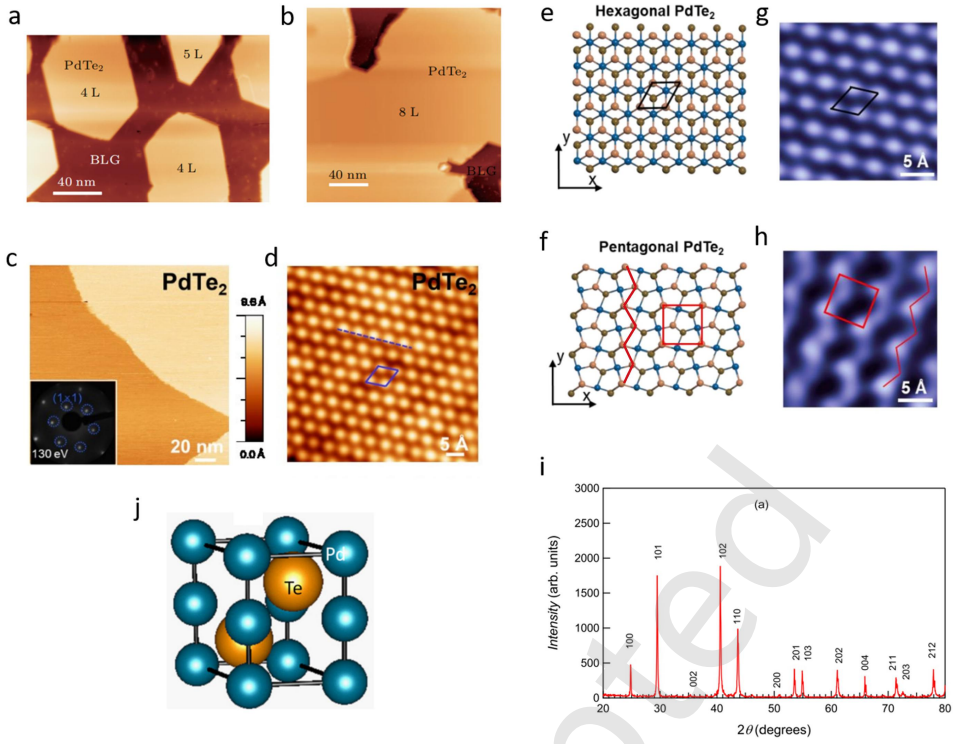

Figure7 (a–b) STM topographic images (1.7 V, 80 pA) of epitaxial $PdTe_2$ films grown on bilayer graphene at (a) low coverage and (b) high coverage. Reproduced with permission. [54] Copyright 2018, the Editorial office of Chinese Physics B. (c–d) (c) STM image of $PdTe_2$. (d) Atomic-resolution STM image of $PdTe_2$. Reproduced with permission. [66] Copyright 2021, IOP Publishing. (e–h) Schematic lattice structures (top view) of (e) monolayer hexagonal $PdTe_2$ and (f) monolayer pentagonal $PdTe_2$. Atomic-resolution STM images of (g) monolayer hexagonal $PdTe_2$ and (h) monolayer pentagonal $PdTe_2$. Black rhombuses and red squares represent unit cells of hexagonal and pentagonal $PdTe_2$, respectively. Red lines indicate zigzag chains formed by topmost Te atoms. Reproduced with permission. [65] Copyright 2024, Springer Nature. (i–j) (i) XRD pattern of PdTe powder. (j) Schematic illustration of the crystal structure of PdTe. Reproduced with permission. [44] Copyright 2012, IOP Publishing.

3.4 From Sulfides to Tellurides

While the individual Pt- and Pd-based chalcogenides exhibit distinct capabilities, analyzing them in isolation can obscure the broader physical continuum that governs this family. A unified perspective reveals that transitioning from sulfides to selenides and ultimately to tellurides represents a systematic modulation of the principal quantum number (n) and atomic mass (Z) of the chalcogen atoms. This compositional evolution strongly influences the delicate balance between bandgap, interlayer coupling, and SOC[99]. Importantly, this chemical trend does not act in isolation; rather, it is intricately coupled with external and structural degrees of freedom—such as layer thickness, epitaxial strain, defect configurations, substrate screening, and crystal symmetry—which collectively define the operational boundaries of each material[100].

A primary consequence of chalcogen substitution is the evolution of interlayer interactions and band structure. As the chalcogen progresses down Group 16 from S (3p) to Se (4p) and Te (5p), the spatial extension and delocalization of the valence p-orbitals increase significantly. First-principles calculations demonstrate that this extended orbital overlap strengthens the out-of-plane orbital hybridization across the van der Waals gap[101]. This helps explain the varying thickness-dependent phase transitions across the family. Sulfides (e.g., PtS_2, PdS_2) possess relatively tightly bound 3p orbitals, generally maintaining a robust semiconducting bandgap even in thicker forms. In contrast, the highly extended 5p orbitals of Te induce stronger interlayer electronic communication, causing $PtTe_2$ and $PdTe_2$ to typically transition into semimetallic states beyond the few-layer limit[26]. Furthermore, this thickness-dependent evolution can be finely tuned by substrate interactions; strong coupling with the underlying substrate can alter local orbital overlap and dielectric screening, thereby shifting the critical thickness required for the semiconductor-to-metal transition[88]. Selenides represent a highly tunable intermediate, offering a broad transition window that is actively sought after for layer-programmable devices.

Parallel to orbital hybridization, the increase in atomic number generally enhances the atomic SOC scale, which, together with changes in orbital hybridization and crystal symmetry, strongly influences the electronic structure. The relatively light sulfur atoms generally result in weaker SOC, making pristine sulfides less favorable for strong SOC-driven topological phenomena[102]. The introduction of heavy tellurium atoms, however, triggers massive SOC effects, which can lead to profound band inversion near the Fermi level[103]. This heavy-atom substitution is a primary reason why three-dimensional Type-II Dirac fermions and robust Rashba splitting are highly prominent in telluride systems. Nevertheless, topological phenomena are not exclusively restricted to heavy tellurides. Structural parameters, particularly crystal symmetry and applied strain, offer alternative pathways to induce topological states. For instance, breaking inversion symmetry via localized strain gradients or employing specific stacking orders can artificially enhance Rashba splitting and trigger topological phase transitions even in lighter transition metal dichalcogenides[104].

These fundamental electronic trends influence the practical trade-offs in device engineering, particularly regarding contact resistance and thermodynamic stability. The decreasing electronegativity from S to Te tends to narrow the bandgap and simultaneously lower the work function, which generally reduces contact Schottky barriers.

While tellurides often form near-ideal Ohmic contacts with standard metals, their weaker metal-chalcogen bonds can reduce their thermal and chemical stability limits compared to their highly refractory sulfide counterparts[105]. Therefore, engineers typically navigate a compromise between maximizing topological and transport efficiency and maintaining processing thermal budgets. However, targeted defect engineering—such as the deliberate introduction of chalcogen vacancies or antisite defects—can strategically alter this balance. By creating mid-gap states or localized magnetic moments, defects can significantly enhance the catalytic or transport characteristics of the more stable sulfides and selenides, partially bridging the performance gap[106].

Looking forward, understanding these systematic trends points toward a clear remaining frontier: compositional alloying and Janus engineering. Rather than selecting discrete binary compounds, recent theoretical and early experimental efforts have demonstrated that ternary alloys (e.g., $PtS_{2-x}Se_x$ or $PdSe_{2-x}Te_x$) and broken-symmetry Janus monolayers (e.g., SPtSe, SePdTe) can continuously interpolate these properties[107, 108]. By intentionally hybridizing the high stability of lighter chalcogens with the strong SOC of heavier chalcogens, researchers can decouple the interdependent relationship between bandgap and topological strength. Combined with precise control over thickness, strain, and substrate symmetry, this compositional tuning paves the way for bespoke 2D materials customized for specific spintronic and photonic requirements.

3.5 Synthesis Conclusion and Outlook

The systematic synthesis of Pt- and Pd-based transition metal chalcogenides has evolved from foundational, vacuum-constrained epitaxial studies to increasingly robust, scalable manufacturing processes. Collectively, these studies reveal that while fundamental properties are dictated by intrinsic structural anisotropy and thickness-dependent stoichiometry, the macroscopic quality and industrial integration of these materials are governed by a complex competition between growth kinetics and thermodynamic phase stability.

Three strategic synthesis paradigms emerge from current literature that define the future of this field. First, for fundamental quantum science, MBE remains particularly valuable, where atomic-scale control of thickness, stoichiometry, and interfaces is essential; the meticulous control over chalcogen-to-metal flux ratios allows for the exploration of metastable phases (e.g., pentagonal $PdTe_2$) and precise band-structure evolution. However, the inherent reliance on expensive, UHV-grade single-crystal substrates presents a significant barrier to practical scaling. Second, for electronic-grade applications, the transition toward TAC and CVD marks a critical paradigm shift. These methods effectively leverage the structural robustness of the Pt/Pd-based chalcogenides, demonstrating that high-quality, continuous, and wafer-scale films can be achieved at thermal budgets strictly compatible with CMOS BEOL constraints (≤400sheshidu). This compatibility uniquely positions this material family to bypass the integration bottlenecks that typically hinder other 2D platforms.

Despite these advancements, critical synthesis-related challenges persist. The primary hurdle remains the mitigation of grain boundaries and structural strain arising from the solid-state transformation of metal precursors, which often manifests as micro-cracking and diminished carrier mobility compared to pristine single-crystalline flakes. Future research must shift from simple morphology optimization toward atomic-level strain-field engineering and grain-boundary passivation. Furthermore, the sensitive chalcogen-desorption equilibrium in these tellurides and selenides demands the development of real-time monitoring and feedback systems during large-area growth to prevent non-stoichiometric defect formation. Conclusively, the successful transition of Pt- and Pd-based chalcogenides from experimental platforms to functional device components depends on our ability to enforce atomic uniformity and phase purity across wafer-scale architectures without sacrificing the unique topological and optoelectronic properties that make these materials scientifically compelling.

To provide a clearer overview of the epitaxial synthesis landscape and to serve as a convenient reference for future experimental designs, the key MBE and direct-epitaxy growth parameters for Pt- and Pd-based dichalcogenides are summarized in Table 1. As illustrated, achieving high-quality two-dimensional or topological phases in these systems typically requires strict control over the substrate temperature and a heavily chalcogen-rich flux environment to suppress thermodynamic vacancy formation.

Table1 Summary of key MBE and epitaxial growth conditions for two-dimensional Pt- and Pd-based dichalcogenides. (T_{sub}: Substrate temperature during growth)

Material	Growth Method	T_{sub} (°C)	Flux Ratio (X/M)	Post-Growth Treatment	Ref.
$PtSe_2$	MBE	~ 280	Se-rich (> 10:1)	-	[138]
$PdSe_2$	MBE	~ 250	Se-rich (> 10:1)	-	[53]
$PtTe_2$	MBE (Stack of monolayer and bilayer)	< 250	Te-rich (> 10:1)	-	[137]
	MBE (Continuous bilayer film)	~ 300	Te-rich (> 10:1)	-	[137]
$PdTe_2$	MBE	~ 250	15:1	-	[54]
	Direct Tellurization	Room Temperature	Direct Te exposure	Annealing at ~ 470°C for 10 mins (Hexagonal)	[66]
	Direct Tellurization	Room Temperature	Direct Te exposure	Annealing at ~ 500°C for 20 mins (Pentagonal)	[65]

4 Material Properties and Device Applications

Two-dimensional Pt- and Pd-based chalcogenides offer broad optoelectronic functionalities spanning the ultraviolet to terahertz regimes, leveraging SOC and thickness-dependent semiconductor-to-semimetal transitions to

4.1 Optoelectronics

surpass the visible-light constraints of conventional group-VI TMDCs.

For near-infrared applications, PdS_2 photodetectors exhibit broadband responses (450-1550nm). Figures 8(a) and 8(b) illustrate the transfer characteristics of a PdS_2 transistor and its photoresponse under 1310nm illumination, achieving a responsivity of 21,5mA W^{-1} and a detectivity of 1.4×10^{10} Jones[109]. Although these metrics are promising, the limited absorption volume of ultrathin films keeps responsivity below commercial InGaAs detectors. Beyond linear absorption, few-layer PdS_2 and $PdSe_2$ demonstrate strong mid-infrared nonlinear absorption. Figures 8(c) and 8(d) depict the stable pulse train and single-pulse profile of a PdS_2-based saturable absorber in an Er:YAP laser, enabling a 525ns pulse width and 93kHz repetition rate[110]. However, minimizing non-saturable losses remains necessary for integration into high-power laser cavities.

Heterostructure and defect engineering provide effective strategies to overcome limited absorption. The PdS_2/PtS_2 vertical van der Waals heterostructure exhibits a Type-II band alignment with small lattice mismatch. Figures 3(h) and 3(i) demonstrate that this configuration red-shifts the optical band gap to 1.5eV and significantly enhances visible-light absorption[48], yielding carrier diffusion lengths exceeding 20μm. At the atomic scale, DFT calculations indicate that Pd vacancies or Mo substitution can induce semimetallic or magnetic semiconducting phases, respectively[49]. Yet, deterministic experimental control is difficult; uncontrolled defects often act as carrier recombination centers, hindering actual device carrier lifetimes despite theoretical predictions.

The physical properties of these materials are deeply rooted in unique interlayer interactions. EELS measurements on PtS_2 ribbons reveal strong Pt-S orbital hybridization, causing the Pt $N_{6,7}$ edge to split into two sharp, layer-dependent peaks as shown in Figure 2(a)[35]. This implies interlayer covalent interactions rather than purely van der Waals coupling, providing superior structural and electrochemical stability. For instance, activated PtS_2 achieves an ultralow HER overpotential of ~60mV at 10mA cm^{-2}[111]. Optically, PtS_2 exhibits ultraviolet absorption, pronounced out-of-plane anisotropy, and a high refractive index (n=3.54 at 800nm), suitable for all-dielectric nanophotonics[112, 113].

As the chalcogen becomes heavier, $PtSe_2$ effectively resolves the contact-resistance bottleneck in 2D electronics, achieving values <700Ω·μm and maintaining room-temperature mobilities around 50$cm^2V^{-1}s^{-1}$[114]. In silicon photonics, TAC-grown $PtSe_2$ on Si waveguides enables CMOS-compatible infrared photodetectors with 11mA W^{-1} responsivity and 8.4μs response time, as shown in Figure 8(e)[44]. Additionally, $PtSe_2/WSe_2/PtSe_2$ junctions provide broadband photoresponse up to 10.6μm[115]. While $PtSe_2$ and $PdSe_2$ offer specific detectivities comparable to black phosphorus with vastly superior air stability[56], their semimetallic thicker layers suffer from higher dark currents, requiring complex heterodiode designs to maintain high signal-to-noise ratios.

The puckered pentagonal lattice of $PdSe_2$ induces strong in-plane anisotropy and unconventional nonlinear optics. Even-layer samples show enhanced SHG, yielding a high second-order nonlinear susceptibility ($\chi^{(2)} = 5.17\times10^{-11}$m/V) and massive two-photon absorption. Figure 8(f) displays the optical images of $PdSe_2$ flakes and the corresponding spatial mapping of the integrated SHG[116]. For high-speed applications, polarization-resolved pump-probe spectroscopy reveals that while thin $PdSe_2$ films undergo rapid intraband hot-carrier cooling, thicker samples (~16.4nm) transition to electron-phonon scattering. Figure 8(g) illustrates these dynamics via time-resolved differential reflectance signals, revealing a pronounced hot-phonon bottleneck effect[117] that mandates the use of few-layer channels to prevent bandwidth degradation.

In integrated sensing, $PdSe_2/WS_2$ devices modulate n-n heterojunction barriers to achieve excellent H_2 detection (67.4% at 50ppm)[118], and $PdSe_2$/Si PIN-like heterojunctions deliver broadband photoresponses[119]. However, commercialization still requires overcoming the ambient cross-sensitivity and sluggish recovery kinetics common in defect-assisted adsorption.

Pushing into the far-infrared, the topological semimetal $PdTe_2$ enables uncooled long-wavelength detection. Mechanically exfoliated $PdTe_2$ flakes act as anisotropic terahertz (THz) phototransistors driven by the photogalvanic effect. Figure 8(h) illustrates the time-resolved response within a single period, showing video-rate response times of 1 and 2.2ms[120]. While this effectively bypasses cryogenic cooling requirements, integrating $PdTe_2$ with plasmonic nanoantennas will be necessary to amplify local fields and overcome the inherently low optical absorption cross-section in the THz band.

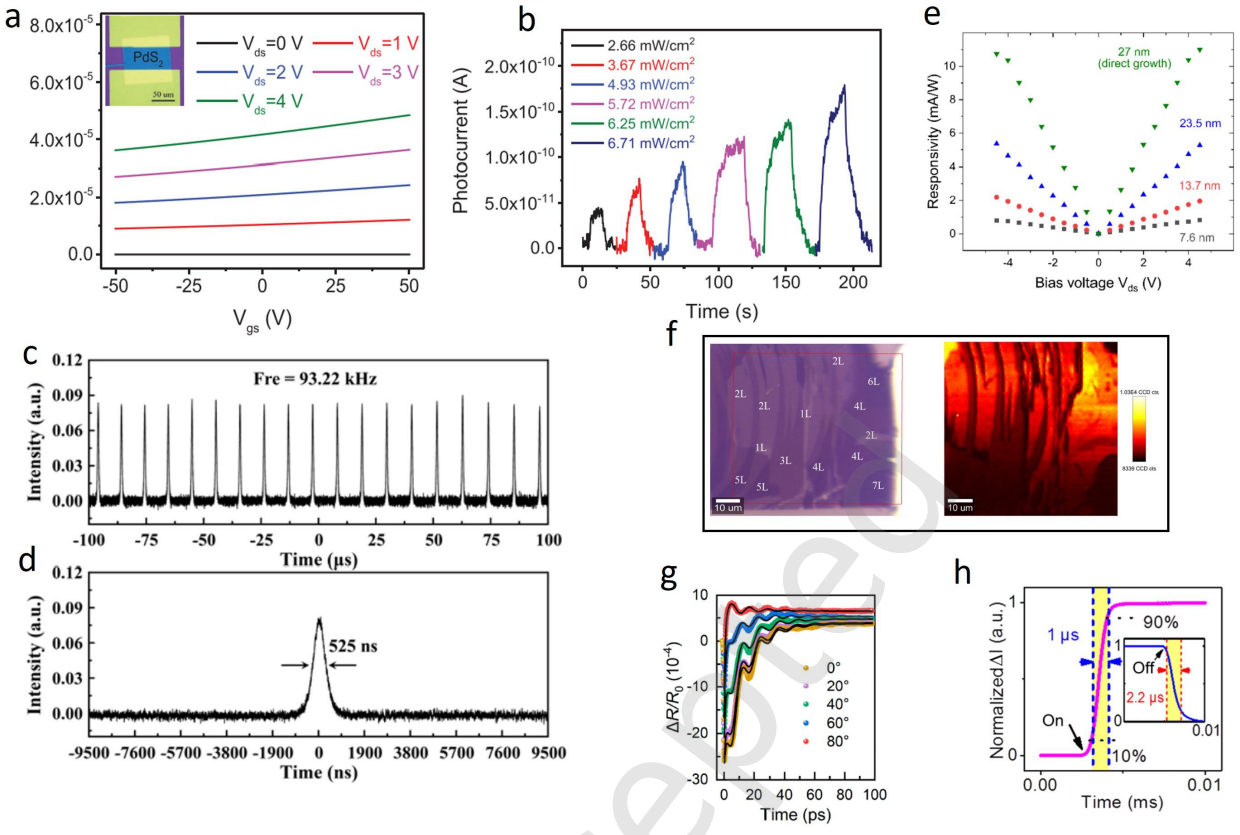

Figure8 (a–b) (a) Transfer characteristics of a PdS_2 field-effect transistor (FET). (b) Photoresponse of PdS_2 films under different power densities with 1310 nm illumination after subtracting the dark current at a bias voltage of 0.01 V. Reproduced with permission. [33] Copyright 2023, John Wiley and Sons. (c–d) (c) Stable PQS pulse train of a PdS_2-SA-based Er:YAP PQS laser. (d) Single-pulse profile of the PdS_2-SA-based Er:YAP PQS laser. Reproduced with permission. [19] Copyright 2025, Optica Publishing Group. (e) Responsivity as a function of bias voltage calculated at a laser output power of 9 mW. Reproduced with permission. [82] Copyright 2022, American Chemical Society. (f) Optical images of $PdSe_2$ flakes for SHG characterization and the corresponding spatial mapping of the integrated SHG signals. Reproduced with permission. [128] Copyright 2021, Springer Nature. (g) Time-resolved differential reflectance signals ($\Delta R/R_0$) as a function of pump–probe delay time at different angles (θ) for a 16.4 nm thick $PdSe_2$ sample, with the angle increased in steps of 20°. Reproduced with permission. [125] Copyright 2024, American Chemical Society. (h) Rising and falling edges of the time-resolved response within a single period, showing a video-rate response time of approximately 1 and 2.2 ms. a.u., arbitrary units. Reproduced with permission. [29] Copyright 2020, the American Association for the Advancement of Science.

4.2 Electronic Transport

Pt- and Pd-based chalcogenides provide versatile platforms for resolving fundamental bottlenecks in two-dimensional transport. Their low-dimensional electronic structures, strong SOC, and structural anisotropy enable transport mechanisms are less readily accessible in conventional high-symmetry group-VI TMDCs.

The heavily puckered pentagonal lattice of semiconducting $PdSe_2$ (~0.5eV gap) breaks spatial symmetry, yielding distinctive axis-dependent conduction polarity (ADCP). Doped $PdSe_2$ exhibits orthogonal n- and p-type conduction at elevated temperatures[121]. DFT links this to complementary carrier effective mass anisotropies: holes have a smaller cross-plane mass (-0.25m_0), while electrons possess lower in-plane masses (0.24-0.26m_0). This strong in-plane anisotropy also drives a pseudo-planar Hall effect (pseudo-PHE) in hBN-encapsulated FETs without an external magnetic field. The gate-tunable, angle-dependent Hall voltage enables reconfigurable XOR/XNOR logic operations while maintaining carrier mobilities up to 210$cm^2V^{-1}s^{-1}$[122].

Suppressing interfacial scattering via hBN encapsulation unlocks high-performance quantum transport in $PdSe_2$. These FETs exhibit room-temperature mobilities around 700$cm^2V^{-1}s^{-1}$, surging to ~$10^4cm^2V^{-1}s^{-1}$ at 2K. Under $B_\perp =$ 12 T , a combined spin and valley quantum octuple degeneracy emerges, which tilted magnetic fields can lift to reveal quantum Hall spin and orbital ferromagnetism. Figure 9(a) illustrates these phenomena through line traces of the resistance $R(V_{tg})$ measured at $B_\perp = 12$ T under different tilting angles, where the traces are offset for clarity and black numbers indicate the corresponding filling factors[123]. This room-temperature mobility surpasses typical few-layer MoS_2 and rivals black phosphorus, yet $PdSe_2$ uniquely avoids rapid ambient degradation[64]. Translating these low-temperature quantum states into functional room-temperature devices, however, requires synthesizing wafer-scale single crystals that match the uniformity of mature GaAs/AlGaAs systems.

Structural anisotropy also strongly scatters phonons, positioning $PdSe_2$ for low-dimensional thermoelectrics. In hBN-encapsulated exfoliated flakes (5-9nm), annealing at 480K increases electron mobility to ~210$cm^2V^{-1}s^{-1}$ and drives conduction from bipolar to n-type. Figure 9(b) presents a power factor comparison between $PdSe_2$ flakes with thicknesses of 5 and 9nm, demonstrating that through thickness optimization, a 5nm flake achieves an enhanced Seebeck coefficient S and power factor PF of approximately 1.5mW $m^{-1}K^{-2}$[124]. Combined with a lattice thermal conductivity of ~4.5W $m^{-1}K^{-1}$, the experimental room-temperature ZT reaches ≈0.1. Theoretically, massive phonon

anharmonicity in $PdSe_2$ monolayers could reduce thermal conductivity to 3.0W $m^{-1}K^{-1}$, projecting room-temperature ZT > 1.1, which is highly competitive with commercial Bi_2Te_3[125]. Reaching these limits requires precise doping to decouple the Seebeck coefficient from electrical conductivity.

A pervasive bottleneck in 2D electronics is severe Fermi-level pinning at metal-semiconductor interfaces. $PtSe_2$ mitigates this issue; fully van der Waals FETs integrating graphite electrodes and hBN dielectrics with $PtSe_2$ channels achieve remarkably low contact resistances[114]. This yields near-ideal Ohmic contacts, heavily outperforming standard Ti/Au contacts on MoS_2 or WSe_2 (typically several kΩ·μm). These devices exhibit on/off ratios of 10^{-9} and mobilities up to 400$cm^2V^{-1}s^{-1}$ at 10K. Moreover, $PtSe_2$ synthesis is BEOL CMOS-compatible, facilitating wafer-scale hybrid logic circuits[114, 44]. Nevertheless, the intrinsic room-temperature mobility of $PtSe_2$ remains heavily phonon-limited (~50$cm^2V^{-1}s^{-1}$), requiring future strain or dielectric engineering to rival the current-drive capabilities of mature silicon or III-V semiconductors.

In the Pd-Te system, bulk $PdTe_2$ operates as a type-I superconductor exhibiting intermediate states and surface superconductivity. The critical magnetic field's temperature dependence deviates from the classical Saint-James-de Gennes relation. Instead, it follows the Werthamer-Helfand-Hohenberg (WHH) model, accounting for orbital depairing, SOC, and Pauli paramagnetism,which indicates unconventional coupling between surface and bulk superconducting states [126].

Thinned to the 2D limit (4-6ML), $PdTe_2$ evolves into a robust Ising-type superconductor. Spin-orbit locking of p_{xy} orbitals near the Γ point enables the in-plane critical magnetic field to exceed the Pauli limit. Figures 9(c) and 9(d) illustrate the parallel magnetic-field dependence of the sheet resistance in a 4ML $PdTe_2$ film at temperatures ranging from 530mK to 1000mK and the R_s(B) curves of a 6 ML film measured from 350mK to 1000mK. Furthermore, Figure 9(e) depicts the in-plane critical field $B_{c\parallel}$ of 4 ML (black spheres) and 6 ML (blue spheres) $PdTe_2$ films. Reaching ~7 times the Pauli limit, $B_{c\parallel}$ in $PdTe_2$ is exceptionally robust compared to canonical 2D superconductors like monolayer $NbSe_2$. Moreover, while $NbSe_2$ oxidizes rapidly, few-layer $PdTe_2$ preserves its superconductivity and topological states after prolonged ambient exposure, resolving a major stability bottleneck for quantum computing architectures[86].

Because the low critical temperature (T_c<1.5K) of pristine $PdTe_2$ restricts operation to dilution refrigerators, interface engineering is utilized to expand its utility. $Bi_2Te_3/PdTe_2$ heterostructures exhibit 2D superconductivity and massive nonreciprocal charge transport under in-plane magnetic fields. Driven by interfacial inversion-symmetry breaking and vortex transitions, these heterostructures demonstrate strong potential for hosting Majorana fermions and realizing fault-tolerant topological superconductivity[127].

4.3 Spintronics

Pt- and Pd-based chalcogenides offer robust platforms for spintronics through three primary mechanisms: defect-induced magnetism, symmetry-driven topological transport, and active spin-charge conversion.

Defect engineering provides a tunable pathway to generate local magnetic moments, circumventing the cryogenic limitations of intrinsic 2D ferromagnets. In $PtSe_2$, DFT calculations indicate that Pt vacancies induce antiferromagnetic ordering in monolayers, which interlayer exchange coupling converts to a ferromagnetic ground state in bilayers. Figures 9(f) and 9(g) illustrate the first-principles calculated localized magnetic moments at Pt-vacancy defects in $PtSe_2$[128]. STM/STS studies corroborate these models, revealing spin-polarized one-dimensional metallic states at zigzag edges. Figure 9(h) illustrates the schematics of five main types of vacancy defects in $PtSe_2$ that serve as magnetic centers[129, 130]. Similar principles apply to PtS_2, where transition metal oxide clusters modulate magnetic moments via orbital hybridization[131]. However, achieving the precise spatial control and uniformity required for practical devices remains a formidable barrier compared to intrinsically magnetic semiconductors.

Beyond localized defects, breaking structural symmetry enables macroscopic topological spin manipulation. Selective plasma etching introduces a gradient of Se vacancies in 1T-$PtSe_2$, breaking spatial inversion symmetry to induce a stable room-temperature Rashba field corresponding to ~4.8T[132]. This symmetry-breaking yields phenomena like angle-sensitive negative magnetoresistance in $PtSe_2$ and de Haas-van Alphen oscillations with nontrivial Berry phases in $PdTe_2$[133, 134]. Yet, studies on intercalated $Cu_{0.05}PdTe_2$ demonstrate that planar Hall effects and anisotropic magnetoresistance can arise purely from extreme anisotropic Fermi surfaces rather than chiral anomalies, indicating that magneto-transport signatures require rigorous corroboration by direct spectroscopic evidence[135].

For active spin-charge conversion, MBE-grown $PtTe_2$ demonstrates massive spin-orbit torque (SOT) effects. Figures 9(i) and 9(j) illustrate the temperature dependence of conductivity in $PtTe_2$ thin films and the thickness dependence of the spin-orbit torque efficiency and spin Hall conductivity. Reaching a spin Hall conductivity up to $0.2-2\times10^5$ $(\hbar/2e)$ Ω^{-1} m^{-1}, $PtTe_2$ rivals canonical heavy metals like Pt and β-Ta while offering CMOS compatibility and robust air stability[136]. Integrating $PtTe_2$ into $PtTe_2/WTe_2$ van der Waals heterostructures transforms the in-plane spin current into an out-of-plane component, enabling deterministic, field-free switching of perpendicular magnetization at room temperature[137].

Dynamic control over these states is achievable in $PtTe_2$/ferromagnet/ferroelectric(PMN-PT) heterostructures, where the substrate's polarization electric field modulates the Fermi level and Berry curvature. Figure 9(k) plots the THz emission amplitude as a function of applied electric field measured over multiple cycles, demonstrating electrically tunable spin Hall conductivity and THz emission[138]. Advancing these conceptual architectures to MRAM commercialization will ultimately require optimizing interfacial transparency and minimizing spin memory loss to fully rival mature heavy-metal systems.

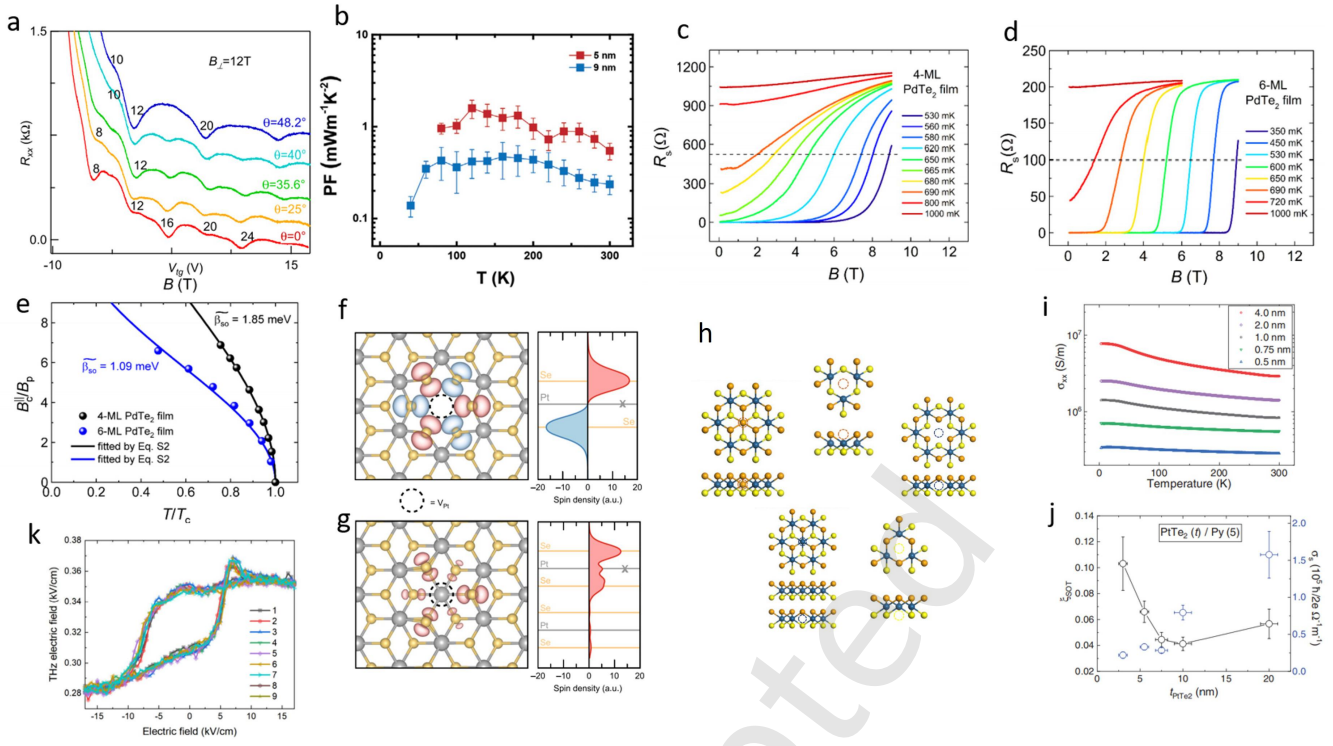

Figure9 (a) Line traces of R(V_{tg}) measured at B⊥ = 12 T under different tilting angles. The traces are offset for clarity. Black numbers indicate the filling factors. Reproduced with permission. [143] Copyright 2024, Springer Nature. (b) Power factor comparison between $PdSe_2$ flakes with thicknesses of 5 and 9 nm. Reproduced with permission. [148] Copyright 2020, John Wiley and Sons. (c–e) (c) Parallel magnetic-field dependence of the sheet resistance in a 4-ML $PdTe_2$ film at different temperatures ranging from 530 mK to 1000 mK. (d) Rs(B) curves of a 6-ML $PdTe_2$ film measured from 350 mK to 1000 mK. (e) In-plane critical field $B_c\|$ of 4-ML (black spheres) and 6-ML (blue spheres) $PdTe_2$ films. Reproduced with permission. [68] Copyright 2020, American Chemical Society. (f–g) First-principles calculated localized magnetic moments at Pt-vacancy defects in $PtSe_2$. Reproduced with permission. [2] Copyright 2020, Springer Nature. (h) Schematics of five main types of vacancy defects in $PtSe_2$. Reproduced with permission. [150] Copyright 2019, IOP Publishing. (i–j) (i) Temperature dependence of conductivity in $PtTe_2$ thin films. (j) Thickness dependence of the spin–orbit torque efficiency ξ_{SOT} and spin Hall conductivity σ_s. Reproduced with permission. [124] Copyright 2020, John Wiley and Sons. (k) THz emission amplitude as a function of applied electric field measured over multiple cycles. Reproduced with permission. [60] Copyright 2025, American Chemical Society.

4.4 Electrocatalysis for Hydrogen Evolution Reaction (HER)

To overcome the catalytic inertness of pristine two-dimensional basal planes, the engineering of Pt- and Pd-based chalcogenides for the HER focuses on lattice expansion, edge-site maximization, and heteroatom doping.

Electrochemical lithium intercalation, for instance, activates $PdSe_2$ by expanding the interlayer spacing and introducing Se vacancies alongside oxygen species. This enhances electrolyte accessibility and boosts oxygen reduction reaction (ORR) activity, positively shifting the half-wave potential by ~250mV and lowering the Tafel slope to 64mV dec^{-1}[139]. DFT calculations confirm that Se vacancies lower intermediate adsorption barriers while strong Pd-Se bonds prevent structural collapse.

Alternatively, maximizing intrinsically active boundaries directly enhances performance. In 1T-phase $PtSe_2$ films grown via magnetron sputtering, adjusting the pre-deposited Pt thickness controls the final edge density, which strongly correlates with HER activity. First-principles calculations verify that both 1T-phase edges ($\Delta G_{H^*} \approx -0.02$ eV) and Se vacancies ($\Delta G_{H^*} \approx 0.13$ eV) serve as primary active sites[140].

To further tune the local electronic environment, heteroatom doping is employed. While $PtTe_2$ provides excellent electrical conductivity, its intrinsic active site density is limited. Introducing Co, Ni, or Fe dopants induces orbital hybridization and tunes the Pt-Te bond strength to optimize hydrogen adsorption. Figures 10(a)-(c) present Tafel slope plots for $PtTe_2$ catalysts under different doping strategies, and Figure 10(d) compares the overpotentials of these doped $PtTe_2$ samples relative to commercial Pt/C [141-143]. As illustrated, these modifications systematically reduce both Tafel slopes and overpotentials.

Ultimately, engineered $PtTe_2$ and $PtSe_2$ achieve ultralow overpotentials of 30-60mV at 10mA cm^{-2}, vastly outperforming 1T-MoS_2 (~90mV) and rivaling commercial 20% Pt/C (30mV). They also maintain stability over 10,000 cyclic voltammetry sweeps without the nanoparticle agglomeration typically observed in Pt/C[144]. However, commercial electrolyzers require current densities exceeding 500mA cm^{-2}. Under such harsh cathodic loads, the specific defects and dopants introduced to activate the basal planes risk becoming sites of structural degradation, remaining a primary hurdle for industrial integration.

4.5 Gas Sensing

Pt- and Pd-based TMDCs bridge the gap between high-power metal-oxide (MOX) sensors and non-selective graphene by offering large, functionalizable surface areas and highly tunable transport properties.

Theoretical models demonstrate that metal dispersion on these basal planes enables effective target gas discrimination. In Ni-dispersed monolayer PdS_2, Ni atoms preferentially adsorb at the T_3 site (-4.11eV), where gases like CO and C_2H_2 induce strong chemisorption and modulate electrical conductivity. Figures 10(e)-10(g) illustrate the corresponding electronic band structures of the Ni-PdS_2 gas adsorption systems for H_2, CO, and C_2H_2, respectively, yielding predicted resistive responses of -40.9% for CO and 261.5% for C_2H_2[145]. However, practical translation requires overcoming the competitive adsorption of ambient

moisture and oxygen, which often masks these idealized target signals.

Experimentally, interface chemical engineering provides a robust route to tune selectivity. Coating $PtSe_2$ with a 2D metal-organic framework (Cu-ZnTPyP) switches the device's selectivity from NO_2 to H_2S, achieving a 200ppb detection limit. Figure 10(h) presents a comparison of the gas-sensing responses of pristine $PtSe_2$ and MOF@$PtSe_2$ toward different gases[146].

Compared to conventional MOX sensors that require 200-400sheshidu to activate surface oxygen species, these large-area $PtSe_2$ films achieve ppb-level detection at room temperature. Paired with low-temperature growth, they are directly compatible with BEOL CMOS processing for low-power Internet of Things (IoT) applications[44, 147]. Yet, surface functionalization introduces its own trade-offs: MOFs and nanoparticles often create complex trapping states that prolong recovery times and induce signal hysteresis. Resolving these kinetic bottlenecks without reverting to energy-intensive micro-heaters is essential for commercial viability.

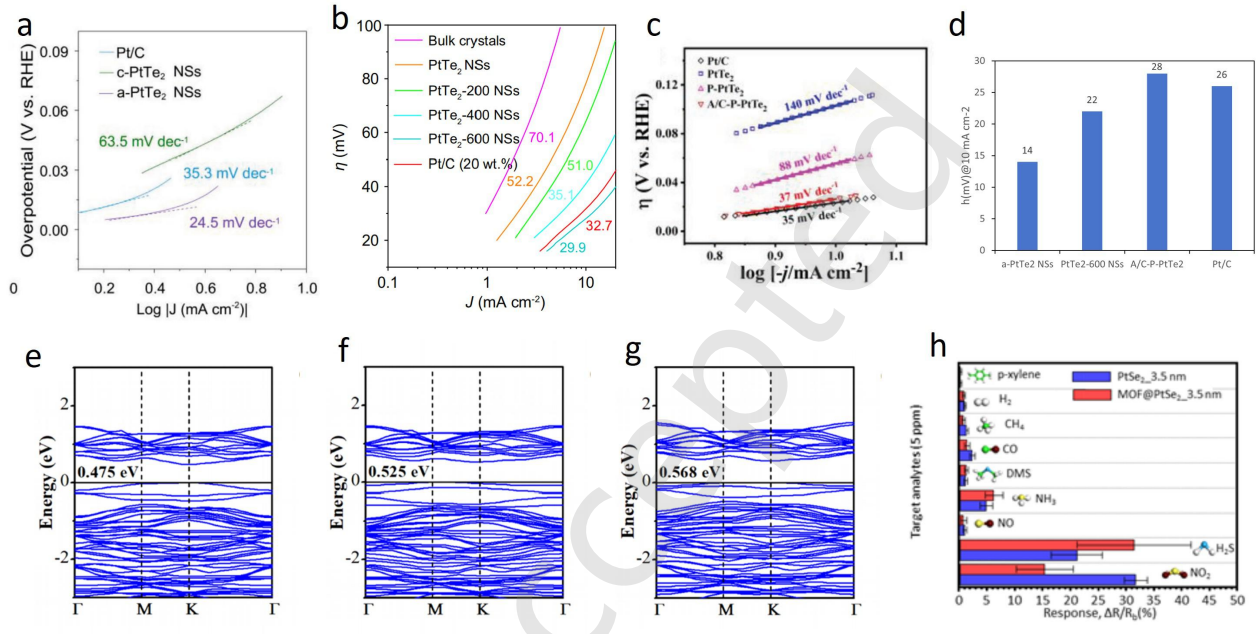

Figure10 (a–c) Tafel slope plots for $PtTe_2$ catalysts under different doping strategies. Reproduced with permission. [145, 71] Copyright 2023, John Wiley and Sons. Reproduced with permission. [58] Copyright 2021, Springer Nature. (d) Comparison of overpotentials for doped $PtTe_2$ samples relative to commercial Pt/C. (e–g) Electronic band structures of Ni–PdS_2/gas adsorption systems: (e) H_2, (f) CO, and (g) C_2H_2. Reproduced with permission. [129] Copyright 2024, American Chemical Society. (h) Comparison of gas-sensing responses of $PtSe_2$ and MOF@$PtSe_2$ toward different gases. Reproduced with permission. [13] Copyright 2022, John Wiley and Sons.

4.6 Other Applications

Pt- and Pd-based chalcogenides are also advancing into structural phase-change devices and neuromorphic computing, with progress spanning from theoretical models to experimental prototypes.

Theoretical studies predict that monolayer PdS_2 forms several penta-structured ferroelastic polymorphs (α, β, γ, δ). The penta-β phase, for instance, promises an electron mobility of ~319$cm^2V^{-1}s^{-1}$ and a low ferroelastic switching barrier of 0.02eV per atom for potential 2D shape-memory devices[148]. At the quasi-1D limit, hydrogen-passivated armchair PdS_2 nanoribbons exhibit tunable transitions among metallic, semiconducting, and magnetic half-metallic states[149]. However, realizing these predicted edge-dependent phases and ferroelastic switches demands atomistic precision in lithography and localized strain control, largely confining these concepts to theoretical exploration.

In contrast, neuromorphic applications have reached experimental realization. CrSBr/PtS_2 van der Waals heterostructures display nonlinear memristive behavior mimicking biological synapses[150]. Compared to conventional transition-metal oxide (e.g., HfO_x) memristors, their atomically thin nature suppresses off-state leakage, driving energy consumption per synaptic spike down to the femtojoule regime, which is highly competitive for next-generation low-power architectures[151]. While these single-device energy metrics are compelling, deploying them in dense neuromorphic arrays requires strict cycle-to-cycle and device-to-device uniformity. Overcoming this fundamental barrier dictates urgent improvements in large-area interface cleanliness and macroscopic defect homogeneity.

5 Conclusion and Outlook

In summary, group-10 transition metal chalcogenides based on Pt and Pd—including sulfides, selenides, and tellurides—exhibit rich and distinctive physical properties in terms of crystal structure, electronic behavior, and functional applications. Owing to their diverse structural configurations, strong SOC, and pronounced thickness-dependent electronic structures, these materials display a variety of band structure evolutions in the two-dimensional limit, ranging from semiconducting to semimetallic and even topological phases. This makes them an important platform for exploring low-dimensional quantum physics and developing novel device functionalities.

From the perspective of material synthesis, MBE, TAC and CVD have become the primary techniques for fabricating high-quality Pt/Pd-based chalcogenide thin films. Among these systems, the MBE growth of selenides and tellurides has already reached a relatively mature stage, while sulfides remain more challenging due to the instability and volatility of sulfur sources under UHV conditions. Nevertheless, strategies such as using FeS_2 as a sulfur source have gradually enabled the controlled epitaxial growth of high-quality sulfide films. By tuning parameters such as growth temperature, flux ratio, precursor thickness, and post-growth treatments, it is possible to precisely control phase formation (e.g., PtS_2/PtS and PdS_2/PdS) and construct various heterostructures, providing a solid experimental foundation for investigating their physical properties.

In terms of intrinsic properties, these two-dimensional chalcogenides exhibit pronounced thickness-dependent band structures, strong light-matter interactions, and rich defect and interface physics. For instance, the electronic structures of materials such as $PtSe_2$, $PdSe_2$, and $PtTe_2$ can be tuned through thickness engineering, enabling transitions from semiconducting to semimetallic or even topological semimetal states. At the same time, the strong SOC in these materials leads to diverse spin-related phenomena, including spin transport effects, spin-orbit torque generation, and Rashba splitting. In addition, various exotic quantum phenomena such as anisotropic charge transport, quantum Hall states, and two-dimensional Ising superconductivity have been observed in these systems, highlighting their importance for fundamental research in low-dimensional quantum materials.

With regard to device applications, Pt/Pd-based chalcogenides have demonstrated broad potential in optoelectronics, spintronics, electronic transport devices, gas sensing, and electrocatalysis. For example, photodetectors based on PdS_2, $PdSe_2$, and $PtSe_2$ can achieve broadband photoresponse ranging from the visible to mid-infrared and even terahertz regimes. Materials such as $PtTe_2$ and $PtSe_2$, owing to their strong SOC and high electrical conductivity, have been identified as efficient spin-orbit torque materials for spintronic devices. In electrocatalysis, defect engineering, edge engineering, and heteroatom doping strategies can significantly enhance the HER activity of $PtSe_2$ and $PtTe_2$. Meanwhile, through interface engineering and surface functionalization, these materials also show promising potential in gas sensing, neuromorphic computing, and flexible electronic devices.

Overall, two-dimensional Pt- and Pd-based chalcogenides provide an important materials platform for studying low-dimensional quantum phenomena and developing next-generation functional devices. Future research directions may focus on several aspects: first, developing more precise and scalable epitaxial growth techniques to achieve atomic-level control of phases and heterostructures; second, systematically exploring the effects of defects, strain, and interfaces on electronic structures and topological properties; and third, advancing practical device implementations in areas such as spintronics, topological electronics, optoelectronic detection, and energy catalysis. With continued progress in synthesis and characterization techniques, Pt/Pd-based two-dimensional chalcogenides are expected to play an increasingly significant role in the development of next-generation quantum materials and advanced functional devices.

Use of AI statement

During the preparation of this work, the author(s) used Chatgpt and Gemini in order to proofread English grammar and polish language in specific sections. After using this tool/service, the author(s) reviewed and edited the content as needed and take(s) full responsibility for the content of the publication.

References

[1] Aslam, M. A., Leitner, S., Tyagi, S., Provias, A., Tkachuk, V., Pavlica, E., Dienstleder, M., Knez, D., Watanabe, K., Taniguchi, T., et al. All van der waals semiconducting $PtSe_2$ field effect transistors with low contact resistance graphite electrodes. Nano Letters 24, 22 (2024), 6529–6537.

[2] Avsar, A., Cheon, C.-Y., Pizzochero, M., Tripathi, M., Ciarrocchi, A., Yazyev, O. V., and Kis, A. Probing magnetism in atomically thin semiconducting $PtSe_2$. Nature communications 11, 1 (2020), 4806.

[3] Bahramy, M., Clark, O., Yang, B.-J., Feng, J., Bawden, L., Riley, J., Marković, I., Mazzola, F., Sunko, V., Biswas, D., et al. Ubiquitous formation of bulk dirac cones and topological surface states from a single orbital manifold in transition-metal dichalcogenides. Nature materials 17, 1

(2018), 21–28.

[4] Bassi, G., Wadhwa, R., Deswal, S., Kumar, P., and Kumar, M. Controlled and tunable growth of ambient stable 2d PtS_2 thin film and its high-performance broadband photodetectors. Journal of Alloys and Compounds 955 (2023), 170233.

[5] Bastonero, L., Cicero, G., Palummo, M., and Re Fiorentin, M. Boosted solar light absorbance in PdS_2 /PtS_2 vertical heterostructures for ultrathin photovoltaic devices. ACS applied materials & interfaces 13, 36 (2021), 43615–43621.

[6] Bhatt, R., Bhattacharya, S., Basu, R., Singh, A., Deshpande, U., Surger, C., Basu, S., Aswal, D., and Gupta, S. Growth of Pd4 S, PdS and PdS_2 films by controlled sulfurization of sputtered pd on native oxide of si. Thin Solid Films 539 (2013), 41–46.

[7] Chapai, R., Browne, D., Graf, D. E., DiTusa, J., and Jin, R. Quantum oscillations with angular dependence in $PdTe_2$ single crystals. Journal of Physics: Condensed Matter 33, 3 (2020), 035601.

[8] Chaves, A., Azadani, J. G., Alsalman, H., Da Costa, D., Frisenda, R., Chaves, A., Song, S. H., Kim, Y. D., He, D., Zhou, J., et al. Bandgap engineering of two-dimensional semiconductor materials. npj 2D Materials and Applications 4, 1 (2020), 29. 18

[9] Chen, C.-F., Huang, T.-C., Wu, P.-T., Chou, Y.-A., Wang, C.-T., Cheng, S.-M., Lin, S.- F., Chen, W.-H., Amrit, P., Kuo, C.-N., et al. All-electric functional $PdSe_2$ planar-hall logic field-effect transistors. Advanced Functional Materials 35, 7 (2025), 2412896.

[10] Chen, S., Ke, S., Ji, T., Li, Z., Xu, X., Liu, B., Huang, Z., Liu, G., and Zhou, J. High-speed self-powered $PdSe_2$ /Si 2d-3d pin-like photodetector with broadband response based on $PdSe_2$ quantum island structure. ACS Applied Materials & Interfaces 16, 32 (2024), 42577–42587.

[11] Chen, Z., Qiu, H., Cheng, X., Cui, J., Jin, Z., Tian, D., Zhang, X., Xu, K., Liu, R., Niu, W., et al. Defect-induced helicity dependent terahertz emission in dirac semimetal $PtTe_2$ thin films. Nature Communications 15, 1 (2024), 2605.

[12] Chia, X., Adriano, A., Lazar, P., Sofer, Z., Luxa, J., and Pumera, M. Layered platinum dichalcogenides (pts_2, $ptse_2$, and $ptte_2$) electrocatalysis: monotonic dependence on the chalcogen size. Advanced Functional Materials 26, 24 (2016), 4306–4318.

[13] Cho, S. R., Kim, D.-H., Jeon, M., Rani, P., Gyeon, M., Kim, Y., Jo, M.-k., Song, S., Park, J. Y., Kim, J., et al. Overlaying monolayer metal–organic framework on $PtSe_2$ -based gas sensor for tuning selectivity. Advanced Functional Materials 32, 47 (2022), 2207265.

[14] Choi, M., Oh, S., Hahn, S., Ji, Y., Jo, M.-k., Kim, J., Ju, T.-S., Kim, G., Gyeon, M., Lee, Y., et al. Wafer-scale synthesis of highly oriented 2d topological semimetal $PtTe_2$ via tellurization. ACS nano 18, 23 (2024), 15154–15166.

[15] Cook, J., Mardanya, S., Lu, Q., Conner, C., Snyder, M., Zhang, X., McMillen, J., Watson, G., Chang, T.-R., and Bian, G. Observation of gapped topological surface states and isolated surface resonances in $PdTe_2$ ultrathin films. Nano letters 23, 5 (2023), 1752–1757.

[16] Cullen, C. P., Coileáin, C. Ó., McManus, J. B., Hartwig, O., McCloskey, D., Duesberg, G. S., and McEvoy, N. Synthesis and characterisation of thin-film platinum disulfide and platinum sulfide. Nanoscale 13, 15 (2021), 7403–7411.

[17] Deng, K., Yan, M., Yu, C.-P., Li, J., Zhou, X., Zhang, K., Zhao, Y., Miyamoto, K., Okuda, T., Duan, W., et al. Crossover from 2d metal to 3d dirac semimetal in metallic $PtTe_2$ films with local rashba effect. Science Bulletin 64, 15 (2019), 1044–1048.

[18] Dong, Z., Yu, W., Zhang, L., Yang, L., Huang, L., Zhang, Y., Ren, Z., Mu, H., Chen, C., Zhang, J., et al. Wafer-scale patterned growth of type-ii dirac semimetal platinum ditelluride for sensitive room-temperature terahertz photodetection. InfoMat 5, 5 (2023), e12403.

[19] Du, B., Pan, H., Pan, Z., Chu, H., Li, Y., Zhao, S., and Li, D. Pd_{X2} (X= S, Se) saturable absorbers for passively q-switched er: Yap laser at 3 μm. Optics Express 33, 14 (2025), 30799–30810.

[20] Du, J., Song, P., Fang, L., Wang, T., Wei, Z., Li, J., and Xia, C. Elastic, electronic and optical properties of the two-dimensional pt_{x2} (x= s, se, and te) monolayer. Applied Surface Science 435 (2018), 476–482.

[21] Du, Y., Zhou, F., Zhang, Y., Zhang, H., Zhang, Y., Zhang, Y., Li, J., Lu, S., Wang, T., Qi, W., et al. On-device synthesis of pdte thin flakes with 2d nature of superconductivity. Advanced Functional Materials (2025), 2425251.

[22] Ermolaev, G. A., Voronin, K. V., Tatmyshevskiy, M. K., Mazitov, A. B., Slavich, A. S., Yakubovsky, D. I., Tselin, A. P., Mironov, M. S., Romanov, R. I., Markeev, A. M., et al. Broadband optical properties of atomically thin PtS_2 and $PtSe_2$. Nanomaterials 11, 12 (2021), 3269.

[23] Ersan, F., and Ataca, C. Janus pt x n y 2- n (x, y= s, se, te; 0 n 2) monolayers for enhanced photocatalytic water splitting. Physical Review Applied 13, 6 (2020), 064008. 19

[24] Feng, R., Zhang, Y., Li, J., Li, Q., Bao, C., Zhang, H., Chen, W., Tang, X., Yaegashi, K., Sugawara, K., et al. Giant rashba splitting in PtTe/$PtTe_2$ heterostructure. Nature Communications 16, 1 (2025), 1–8.

[25] Fu, D., Zhao, X., Zhang, Y.-Y., Li, L., Xu, H., Jang, A.-R., Yoon, S. I., Song, P., Poh, S. M., Ren, T., et al. Molecular beam epitaxy of highly crystalline monolayer molybdenum disulfide on hexagonal boron nitride. Journal of the American Chemical Society 139, 27 (2017), 9392–9400.

[26] Gan, Y., Quhe, R., Wu, L., Hou, S., Bi, J., Liu, G., and Lu, P. Structural and electronic properties of PdS_2 nanoribbons. Journal of Magnetism and Magnetic Materials 458 (2018), 310–316.

[27] Gao, H., Zhou, H., Hao, Y., Zhou, G., Zhou, H., Gao, F., Xiao, J., Tang, P., and Hao, G. Controllable growth of wafer-scale PdS and PdS_2 nanofilms via chemical vapor deposition combined with an electron beam evaporation technique. Journal of Semiconductors 44, 12 (2023), 122001.

[28] Ghanipour, A., Han, S. S., Yoo, C., Lee, C. W., and Jung, Y. Introducing semiconducting-to- metallic transitions into wafer-scale 2d $pdse_2$ layers by low-temperature anion exchange and thickness modulation. ACS nano 18, 52 (2024), 35336–35346.

[29] Guo, C., Hu, Y., Chen, G., Wei, D., Zhang, L., Chen, Z., Guo, W., Xu, H., Kuo, C.-N., Lue, C. S., et al. Anisotropic ultrasensitive $PdTe_2$ -based phototransistor for room-temperature long-wavelength detection. Science Advances 6, 36 (2020), eabb6500.

[30] Ha, C., and Chung, Y. J. Thin films as practical quantum materials: A status quo and beyond. APL Materials 12, 12 (2024).

[31] Hall, J., Pielić, B., Murray, C., Jolie, W., Wekking, T., Busse, C., Kralj, M., and Michely, T. Molecular beam epitaxy of quasi-freestanding transition metal disulphide monolayers on van der waals substrates: a growth study. 2D Materials 5, 2 (2018), 025005.

[32] He, J., Jiang, W., Zhu, X., Zhang, R., Wang, J., Zhu, M., Wang, S., Zheng, Y., and Chen, L. Optical properties of thickness-controlled $PtSe_2$ thin films studied via spectroscopic ellipsometry. Physical Chemistry Chemical Physics 22, 45 (2020), 26383–26389.

[33] He, K., Xu, W., Tang, J., Lu, Y., Yi, C., Li, B., Zhu, H., Zhang, H., Lin, X., Feng, Y., et al. Centimeter-scale PdS_2 ultrathin films with high mobility and broadband photoresponse. Small 19, 17 (2023), 2206915.

[34] He, L., Lv, H., Ma, L., Li, W., Si, J., Ikram, M., Ullah, M., Wu, H., Wang, R., and Shi, K. Controllable synthesis of intercalated γ-bi_2moo_6/graphene nanosheet composites for high performance no_2 gas sensor at room temperature. Carbon 157 (2020), 22–32.

[35] Hidding, J., and Guimarães, M. H. Spin-orbit torques in transition metal dichalco- genide/ferromagnet heterostructures. Frontiers in Materials 7 (2020), 594771.

[36] Hilse, M., Wang, K., and Engel-Herbert, R. Growth of ultrathin pt layers and selenization into $PtSe_2$ by molecular beam epitaxy. 2D Materials 7, 4 (2020), 045013.

[37] Hilse, M., Wang, K., and Engel-Herbert, R. Molecular beam epitaxy of $PtSe_2$ using a co- deposition approach. 2D Materials 9, 2 (2022), 025029.

[38] Hoffman, A. N., Gu, Y., Liang, L., Fowlkes, J. D., Xiao, K., and Rack, P. D. Exploring the air stability of $pdse_2$ via electrical transport measurements and defect calculations. npj 2D Materials and Applications 3, 1 (2019), 50.

[39] Hooda, M., Sharma, S., Yadav, C., et al. Planar hall effect in cu intercalated $PdTe_2$. Applied Physics Letters 119, 26 (2021).

[40] Huh, W., Lee, D., and Lee, C.-H. Memristors based on 2d materials as an artificial synapse for neuromorphic electronics. Advanced materials 32, 51 (2020), 2002092. 20

[41] Jadwiszczak, J., Kelly, D. J., Guo, J., Zhou, Y., and Zhang, H. Plasma treatment of ultrathin layered semiconductors for electronic device applications. ACS Applied Electronic Materials 3, 4 (2021), 1505–1529.

[42] Jiang, S., Yang, J., Zhu, L., Xie, J., Guo, W., Zhao, E., Chen, C., Wang, T., Su, F., Zhang, Y., et al. Nonlinear electronic and ultrafast optical signatures in chemical vapor-deposited ultrathin PtS_2 ribbons. Nano Research 15, 5 (2022), 4366–4373.

[43] Jo, J., Kim, J. H., Kim, C. H., Lee, J., Choe, D., Oh, I., Lee, S., Lee, Z., Jin, H., and Yoo, J.-W. Defect-gradient-induced rashba effect in van der waals $PtSe_2$ layers. Nature Communications 13, 1 (2022), 2759.

[44] Karki, A., Browne, D., Stadler, S., Li, J., and Jin, R. Pdte: a strongly coupled superconductor. Journal of Physics: Condensed Matter 24, 5 (2012),

055701.

[45] Khan, M. A., Khan, M. F., Nasim, M., Elahi, E., Rabeel, M., Asim, M., Rehmat, A., Pervez, M. H., Rehman, S., Kim, H., et al. Photonic synapse of CrSBr/PtS_2 transistor for neuromorphic computing and light decoding. Advanced Functional Materials 34, 52 (2024), 2410974.

[46] Khan, M. Y., Usman, T., Ilyas, A., Hassan, A., Younis, U., Ullah, A., Ahmad, S. A., and Al Souwaileh, A. Electronic, optical, and magnetic properties of defect-engineered 1t-PdS_2 monolayer: A first-principles investigation. Materials Science in Semiconductor Processing 187 (2025), 109144.

[47] Kim, H. J., Choi, B. K., Lee, I. H., Kim, M. J., Chun, S.-H., Jozwiak, C., Bostwick, A., Rotenberg, E., and Chang, Y. J. Electronic structure and charge-density wave transition in monolayer vs2. Current Applied Physics 30 (2021), 8–13.

[48] Koh, S. W., Hu, J., Hwang, J., Yu, P., Sun, Z., Liu, Q., Hong, W., Ge, J., Fei, J., Han, B., et al. Two-dimensional palladium diselenide for the oxygen reduction reaction. Materials Chemistry Frontiers 5, 13 (2021), 4970–4980.

[49] Kumar, S., Kumar, A., Kumar, A., Chakkar, A. G., Betal, A., Kumar, P., Sahu, S., and Kumar, M. Catalytic synergy of WS_2 -anchored $PdSe_2$ for highly sensitive hydrogen gas sensor. Nanoscale 16, 19 (2024), 9593–9602.

[50] Lasek, K., Ghorbani-Asl, M., Pathirage, V., Krasheninnikov, A. V., and Batzill, M. Controlling stoichiometry in ultrathin van der waals films: $PtTe_2$, Pt2 Te3 , Pt3 Te4 , and Pt2 Te2 . ACS nano 16, 6 (2022), 9908–9919.

[51] Lasek, K., Li, J., Ghorbani-Asl, M., Khatun, S., Alanwoko, O., Pathirage, V., Krasheninnikov, A. V., and Batzill, M. Formation of in-plane semiconductor–metal contacts in 2d platinum telluride by converting $PtTe_2$ to Pt2 Te2 . Nano Letters 22, 23 (2022), 9571–9577.

[52] Leng, H., Paulsen, C., Huang, Y., and De Visser, A. Type-i superconductivity in the dirac semimetal $PdTe_2$. Physical Review B 96, 22 (2017), 220506.

[53] Li, E., Wang, D., Fan, P., Zhang, R., Zhang, Y.-Y., Li, G., Mao, J., Wang, Y., Lin, X., Du, S., et al. Construction of bilayer $PdSe_2$ on epitaxial graphene. Nano Research 11, 11 (2018), 5858–5865.

[54] Li, E., Zhang, R.-Z., Li, H., Liu, C., Li, G., Wang, J.-O., Qian, T., Ding, H., Zhang, Y.-Y., Du, S.-X., et al. High quality $PdTe_2$ thin films grown by molecular beam epitaxy. Chinese Physics B 27, 8 (2018), 086804.

[55] Li, J., Joseph, T., Ghorbani-Asl, M., Kolekar, S., Krasheninnikov, A. V., and Batzill, M. Edge and point-defect induced electronic and magnetic properties in monolayer $PtSe_2$. Advanced Functional Materials 32, 18 (2022), 2110428. 21

[56] Li, J., Kolekar, S., Ghorbani-Asl, M., Lehnert, T., Biskupek, J., Kaiser, U., Krashenin- nikov, A. V., and Batzill, M. Layer-dependent band gaps of platinum dichalcogenides. ACS Nano 15, 8 (2021), 13249–13259.

[57] Li, J., Zhang, R.-Z., Pan, J., Chen, P., and Du, S. Emergence of metal–semiconductor phase transition in M_{X2} (M= Ni, Pd, Pt; X= S, Se, Te) moiré superlattices. Chinese Physics B 34, 3 (2025), 037302.

[58] Li, X., Fang, Y., Wang, J., Fang, H., Xi, S., Zhao, X., Xu, D., Xu, H., Yu, W., Hai, X., et al. Ordered clustering of single atomic te vacancies in atomically thin $PtTe_2$ promotes hydrogen evolution catalysis. Nature Communications 12, 1 (2021), 2351.

[59] Li, Z., Huang, M., Li, J., and Zhu, H. Large-scale, controllable synthesis of ultrathin platinum diselenide ribbons for efficient electrocatalytic hydrogen evolution. Advanced Functional Materials 33, 28 (2023), 2300376.

[60] Li, Z., Yang, D., Wang, F., Yang, Y., Guo, Y., Bao, D., Yin, T., Tang, C. S., Salim, T., Xi, L., et al. Electric-field tunable thz emission via quantum geometry in dirac semimetal. Nano Letters 25, 22 (2025), 9006–9014.

[61] Liao, Y.-S., Wang, R.-Y., Tsai, H.-W., Chen, G.-H., Chan, H.-H., Hsieh, H.-T., Cheng, C.-M., Lin, C.-L., Lin, M.-K., and Chou, J.-P. Moiré-induced electronic reconstruction in van der waals heterobilayer $PtSe_2$ /$PtTe_2$. ACS nano (2026).

[62] Lin, S., Liu, Y., Hu, Z., Lu, W., Mak, C. H., Zeng, L., Zhao, J., Li, Y., Yan, F., Tsang, Y. H., et al. Tunable active edge sites in $PtSe_2$ films towards hydrogen evolution reaction. Nano Energy 42 (2017), 26–33.

[63] Lin, Z., Carvalho, B. R., Kahn, E., Lv, R., Rao, R., Terrones, H., Pimenta, M. A., and Terrones, M. Defect engineering of two-dimensional transition metal dichalcogenides. 2D Materials 3, 2 (2016), 022002.

[64] Liu, C., Lian, C.-S., Liao, M.-H., Wang, Y., Zhong, Y., Ding, C., Li, W., Song, C.-L., He, K., Ma, X.-C., et al. Two-dimensional superconductivity and topological states in $PdTe_2$ thin films. Physical Review Materials 2, 9 (2018), 094001.

[65] Liu, L., Ji, Y., Bianchi, M., Hus, S. M., Li, Z., Balog, R., Miwa, J. A., Hofmann, P., Li, A.- P., Zemlyanov, D. Y., et al. A metastable pentagonal 2d material synthesized by symmetry-driven epitaxy. Nature Materials 23, 10 (2024), 1339–1346.

[66] Liu, L., Zemlyanov, D., and Chen, Y. P. Epitaxial growth of monolayer $PdTe_2$ and patterned $PtTe_2$ by direct tellurization of pd and pt surfaces. 2D Materials 8, 4 (2021), 045033.

[67] Liu, W., Osanloo, M. R., Wang, X., Li, S., Dhale, N., Wu, H., Van de Put, M. L., Tiwari, S., Vandenberghe, W. G., and Lv, B. New verbeekite-type polymorphic phase and rich phase diagram in the pdse $_2$- x te x system. Physical Review B 104, 2 (2021), 024507.

[68] Liu, Y., Xu, Y., Sun, J., Liu, C., Liu, Y., Wang, C., Zhang, Z., Gu, K., Tang, Y., Ding, C., et al. Type-ii ising superconductivity and anomalous metallic state in macro-size ambient-stable ultrathin crystalline films. Nano letters 20, 8 (2020), 5728–5734.

[69] Lu, J., Zhang, X., Su, G., Yang, W., Han, K., Yu, X., Wan, Y., Wang, X., and Yang, P. Large-area uniform few-layer PtS_2 : Synthesis, structure and physical properties. Materials Today Physics 18 (2021), 100376.

[70] Lu, L.-S., Chen, G.-H., Cheng, H.-Y., Chuu, C.-P., Lu, K.-C., Chen, C.-H., Lu, M.-Y., Chuang, T.-H., Wei, D.-H., Chueh, W.-C., et al. Layer-dependent and in-plane anisotropic properties of low-temperature synthesized few-layer $PdSe_2$ single crystals. ACS nano 14, 4 (2020), 4963–4972. 22

[71] Ma, H., Huang, X., Li, L., Peng, W., Lin, S., Ding, Y., and Mai, L. Boosting the hydrogen evolution reaction performance of p-doped $PtTe_2$ nanocages via spontaneous defects formation. Small 19, 41 (2023), 2302685.

[72] Manzeli, S., Ovchinnikov, D., Pasquier, D., Yazyev, O. V., and Kis, A. 2d transition metal dichalcogenides. Nature Reviews Materials 2, 8 (2017), 17033.

[73] Masuko, M., Kawamura, M., Yoshimi, R., Hirayama, M., Ikeda, Y., Watanabe, R., He, J. J., Maryenko, D., Tsukazaki, A., Takahashi, K. S., et al. Nonreciprocal charge transport in topological superconductor candidate Bi2 Te3 /$PdTe_2$ heterostructure. npj Quantum Materials 7, 1 (2022), 104.

[74] Matthias, B. Superconducting compounds of nonsuperconducting elements. Physical Review 90, 3 (1953), 487.

[75] Mounet, N., Gibertini, M., Schwaller, P., Campi, D., Merkys, A., Marrazzo, A., Sohier, T., Castelli, I. E., Cepellotti, A., Pizzi, G., et al. Two-dimensional materials from high- throughput computational exfoliation of experimentally known compounds. Nature nanotechnology 13, 3 (2018), 246–252.

[76] Murray, C., Jolie, W., Fischer, J. A., Hall, J., van Efferen, C., Ehlen, N., Grüneis, A., Busse, C., and Michely, T. Comprehensive tunneling spectroscopy of quasifreestanding MoS_2 on graphene on ir (111). Physical Review B 99, 11 (2019), 115434.

[77] Naghavi, S. S., He, J., Xia, Y., and Wolverton, C. Pd2 Se3 monolayer: a promising two- dimensional thermoelectric material with ultralow lattice thermal conductivity and high power factor. Chemistry of Materials 30, 16 (2018), 5639–5647.

[78] Nakano, M., Wang, Y., Kashiwabara, Y., Matsuoka, H., and Iwasa, Y. Layer-by-layer epitaxial growth of scalable WSe_2 on sapphire by molecular beam epitaxy. Nano letters 17, 9 (2017), 5595–5599.

[79] Nelson, R. A., Deng, Z., Ochs, A. M., Koster, K. G., Irvine, C. T., Heremans, J. P., Windl, W., and Goldberger, J. E. Axis dependent conduction polarity in the air-stable semicon- ductor, $PdSe_2$. Materials Horizons 10, 9 (2023), 3740–3748.

[80] Oyedele, A. D., Yang, S., Liang, L., Puretzky, A. A., Wang, K., Zhang, J., Yu, P., Pudasaini, P. R., Ghosh, A. W., Liu, Z., et al. $Pdse_2$: pentagonal two-dimensional layers with high air stability for electronics. Journal of the American Chemical Society 139, 40 (2017), 14090– 14097.

[81] Pandey, L., Kumar, N., Khan, A., Gupta, N. K., Hait, S., Barwal, V., Mishra, V., Sharma, N., and Chaudhary, S. Growth and characterization of the sputtered type-ii topological semimetal $PdTe_2$ thin films and $PdTe_2$ /Co60 Fe20 B20 heterostructures. Journal of Magnetism and Magnetic Materials 584 (2023), 171075.

[82] Parhizkar, S., Prechtl, M., Giesecke, A. L., Suckow, S., Wahl, S., Lukas, S., Hartwig, O., Negm, N., Quellmalz, A., Gylfason, K., et al. Two-dimensional platinum diselenide waveguide-integrated infrared photodetectors. ACS photonics 9, 3 (2022), 859–867.

[83] Pavlosiuk, O., and Kaczorowski, D. Galvanomagnetic properties of the putative type-ii dirac semimetal $PtTe_2$. Scientific Reports 8, 1 (2018), 11297.

[84] Perini, C. J., Muller, M. J., Wagner, B. K., and Vogel, E. M. Low-temperature, plasma assisted, cyclic synthesis of mos_2. Journal of Vacuum Science & Technology B 36, 3 (2018).

[85] Pi, L., Li, L., Hu, X., Zhou, S., Li, H., and Zhai, T. Temperature dependence of raman responses of few-layer pts_2. Nanotechnology 29, 50 (2018), 505709. 23

[86] Pi, L., Li, L., Liu, K., Zhang, Q., Li, H., and Zhai, T. Recent progress on 2d noble-transition- metal dichalcogenides. Advanced Functional Materials 29, 51 (2019), 1904932.

[87] Priyanka, Chowdhury, S., Ritu, Kumar, V., Kumar, R., and Chand, F. Detailed investiga- tions on stability and optoelectronic characteristics of the 1t-PdS_2 monolayer. Physica Scripta 99, 2 (2024), 025945.

[88] Qian, X., Liu, J., Fu, L., and Li, J. Quantum spin hall effect in two-dimensional transition metal dichalcogenides. Science 346, 6215 (2014), 1344–1347.

[89] Qin, D., Yan, P., Ding, G., Ge, X., Song, H., and Gao, G. Monolayer $pdse_2$: A promising two-dimensional thermoelectric material. Scientific reports 8, 1 (2018), 2764.

[90] Roy, S., Joseph, A., Zhang, X., Bhattacharyya, S., Puthirath, A. B., Biswas, A., Tiwary, C. S., Vajtai, R., and Ajayan, P. M. Engineered two-dimensional transition metal dichalcogenides for energy conversion and storage. Chemical Reviews 124, 16 (2024), 9376–9456.

[91] Ryu, G. H., Chen, J., Wen, Y., and Warner, J. H. In-situ atomic-scale dynamics of thermally driven phase transition of 2d few-layered 1t $PtSe_2$ into ultrathin 2d nonlayered PtSe crystals. Chemistry of Materials 31, 23 (2019), 9895–9903.

[92] Ryu, J. H., Lee, K. H., Hong, S.-w., Hwang, J. Y., Yi, Y., Im, S., Kim, S.-i., Kim, S. Y., and Lee, K. Compositional effect in pentagonal layered $PdSe_{2-x}$ Sx solid-solutions and their transport properties. Scripta Materialia 182 (2020), 6–10.

[93] Sant, R., Gay, M., Marty, A., Lisi, S., Harrabi, R., Vergnaud, C., Dau, M. T., Weng, X., Coraux, J., Gauthier, N., et al. Synthesis of epitaxial monolayer janus SPtSe. npj 2D Materials and Applications 4, 1 (2020), 41.

[94] Shao, Q., Yu, G., Lan, Y.-W., Shi, Y., Li, M.-Y., Zheng, C., Zhu, X., Li, L.-J., Amiri, P. K., and Wang, K. L. Strong rashba-edelstein effect-induced spin–orbit torques in monolayer transition metal dichalcogenide/ferromagnet bilayers. Nano letters 16, 12 (2016), 7514–7520.

[95] Sharma, V., and Jha, P. K. Investigating the lattice dynamics and electronic structure of monolayer $PdTe_2$. In AIP Conference Proceedings (2020), vol. 2265, AIP Publishing LLC, p. 030719.

[96] Shawkat, M. S., Hafiz, S. B., Islam, M. M., Mofid, S. A., Al Mahfuz, M. M., Biswas, A., Chung, H.-S., Okogbue, E., Ko, T.-J., Chanda, D., et al. Scalable van der waals two- dimensional $PtTe_2$ layers integrated onto silicon for efficient near-to-mid infrared photodetection. ACS applied materials & interfaces 13, 13 (2021), 15542–15550.

[97] Song, S., Oh, I., Jang, S., Yoon, A., Han, J., Lee, Z., Yoo, J.-W., and Kwon, S.-Y. Air-stable van der waals $PtTe_2$ conductors with high current-carrying capacity and strong spin-orbit interaction. Iscience 25, 11 (2022).

[98] Song, X., Liu, Q., Yu, B., Dubois, D., and Chen, S. Stabilization and surface functionalization of palladium disulfide nanoparticles with acetylene derivatives. Langmuir 40, 42 (2024), 22394–22400.

[99] Sorokin, S. V., Avdienko, P. S., Sedova, I. V., Kirilenko, D. A., Davydov, V. Y., Komkov, O. S., Firsov, D. D., and Ivanov, S. V. Molecular beam epitaxy of layered group iii metal chalcogenides on gaas (001) substrates. Materials 13, 16 (2020), 3447.

[100] Su, H., Zheng, Z., Yu, Z., Feng, S., Lan, H., Wang, S., Zhang, M., Li, L., and Liang, H. Optically controlling broadband terahertz modulator based on layer-dependent $PtSe_2$ nanofilms. Nanomaterials 13, 5 (2023), 795.

[101] Sun, J., Deacon, R. S., Luo, W., Yuan, Y., Liu, X., Xie, H., Gao, Y., and Ishibashi, K. Asymmetric fermi velocity induced chiral magnetotransport anisotropy in the type-ii dirac semi-metal $PtSe_2$. Communications Physics 3, 1 (2020), 93. 24

[102] Tai, K.-L., Chen, J., Wen, Y., Park, H., Zhang, Q., Lu, Y., Chang, R.-J., Tang, P., Allen, C. S., Wu, W.-W., et al. Phase variations and layer epitaxy of 2d $PdSe_2$ grown on 2d monolayers by direct selenization of molecular Pd precursors. ACS nano 14, 9 (2020), 11677–11690.

[103] Tien, N. T., Guerrero-Sanchez, J., and Hoat, D. A systematic study of TMO_n (TM= V, Cr, Mn, and Fe; n= 3 and 6) clusters embedded in a PtS_2 monolayer. Nanoscale Advances 6, 22 (2024), 5671–5680.

[104] Tong, Y., Bouaziz, M., Oughaddou, H., Enriquez, H., Chaouchi, K., Nicolas, F., Kubsky, S., Esaulov, V., and Bendounan, A. Phase transition and thermal stability of epitaxial $PtSe_2$ nanolayer on Pt (111). RSC advances 10, 51 (2020), 30934–30943.

[105] Ugeda, M. M., Bradley, A. J., Shi, S.-F., Da Jornada, F. H., Zhang, Y., Qiu, D. Y., Ruan, W., Mo, S.-K., Hussain, Z., Shen, Z.-X., et al. Giant bandgap renormalization and excitonic effects in a monolayer transition metal dichalcogenide semiconductor. Nature materials 13, 12 (2014), 1091–1095.

[106] Valerius, P., Kretschmer, S., Senkovskiy, B. V., Wu, S., Hall, J., Herman, A., Ehlen, N., Ghorbani-Asl, M., Grueneis, A., Krasheninnikov, A. V., et al. Reversible crystalline-to- amorphous phase transformation in monolayer MoS_2 under grazing ion irradiation. 2D Materials 7, 2 (2020), 025005.

[107] van Efferen, C., Hall, J., Atodiresei, N., Boix, V., Safeer, A., Wekking, T., Vinogradov, N. A., Preobrajenski, A. B., Knudsen, J., Fischer, J., et al. 2d vanadium sulfides: Synthesis, atomic structure engineering, and charge density waves. ACS nano 18, 22 (2024), 14161–14175.

[108] Villaos, R. A. B., Crisostomo, C. P., Huang, Z.-Q., Huang, S.-M., Padama, A. A. B., Albao, M. A., Lin, H., and Chuang, F.-C. Thickness dependent electronic properties of pt dichalcogenides. npj 2D Materials and Applications 3, 1 (2019), 2.

[109] Vishwanath, S., Liu, X., Rouvimov, S., Basile, L., Lu, N., Azcatl, A., Magno, K., Wal- lace, R. M., Kim, M., Idrobo, J.-C., et al. Controllable growth of layered selenide and telluride heterostructures and superlattices using molecular beam epitaxy. Journal of Materials Research 31, 7 (2016), 900–910.

[110] Wang, D., Ju, W., Kang, D., Li, T., and Li, H. Tunable electronic, optical, and spintronic properties in InSe/MTe_2 (M= Pd, Pt) van der waals heterostructures. Vacuum 183 (2021), 109859.

[111] Wang, F., Shi, G., Kim, K.-W., Park, H.-J., Jang, J. G., Tan, H. R., Lin, M., Liu, Y., Kim, T., Yang, D., et al. Field-free switching of perpendicular magnetization by two-dimensional $PtTe_2$ /WTe2 van der waals heterostructures with high spin hall conductivity. Nature materials 23, 6 (2024), 768–774.

[112] Wang, H., Zhang, J., Su, G., Lu, J., Wan, Y., Yu, X., and Yang, P. The growth mechanism of PtS_2 single crystal. The Journal of Chemical Physics 160, 13 (2024).

[113] Wang, M., Ko, T.-J., Shawkat, M. S., Han, S. S., Okogbue, E., Chung, H.-S., Bae, T.-S., Sattar, S., Gil, J., Noh, C., et al. Wafer-scale growth of 2d $PtTe_2$ with layer orientation tunable high electrical conductivity and superior hydrophobicity. ACS Applied Materials & Interfaces 12, 9 (2020), 10839–10851.

[114] Wang, Y., Li, L., Yao, W., Song, S., Sun, J., Pan, J., Ren, X., Li, C., Okunishi, E., Wang, Y.-Q., et al. Monolayer $PtSe_2$, a new semiconducting transition-metal-dichalcogenide, epitaxially grown by direct selenization of Pt. Nano letters 15, 6 (2015), 4013–4018.

[115] Wang, Y., Li, Y., and Chen, Z. Not your familiar two dimensional transition metal disulfide: structural and electronic properties of the PdS_2 monolayer. Journal of Materials Chemistry C 3, 37 (2015), 9603–9608. 25

[116] Wang, Y., Szokolova, K., Nasir, M. Z. M., Sofer, Z., and Pumera, M. Layered crystalline and amorphous platinum disulfide (pts_2): Contrasting electrochemistry. Chemistry–A European Journal 25, 30 (2019), 7330–7338.

[117] Wang, Y., Zhang, Y., Cheng, Q., Pang, J., Chu, Y., Ji, H., Gao, J., Han, Y., Han, L., Liu, H., et al. Large area uniform PtS_x synthesis on sapphire substrate for performance improved photodetectors. Applied Materials Today 25 (2021), 101176.

[118] Wei, M., Lian, J., Zhang, Y., Wang, C., Wang, Y., and Xu, Z. Layer-dependent optical and dielectric properties of centimeter-scale $PdSe_2$ films grown by chemical vapor deposition. npj 2D Materials and Applications 6, 1 (2022), 1.

[119] Wu, C.-H., Huang, Y.-C., Ho, Y.-T., Chang, S.-J., Wu, S.-K., Huang, C.-H., Chou, W.-C., and Yang, C.-S. Solid phase epitaxy of single phase two-dimensional layered InSe grown by mbe. Nanomaterials 12, 14 (2022), 2435.

[120] Wu, X., Shao, Y., Liu, H., Feng, Z., Wang, Y.-L., Sun, J.-T., Liu, C., Wang, J.-O., Liu, Z.-L., Zhu, S.-Y., et al. Epitaxial growth and air-stability of monolayer antimonene on $PdTe_2$. Advanced Materials 29, 11 (2017), 1605407.

[121] Xiang, L., Ke, Y., and Zhang, Q. Tunable giant rashba-type spin splitting in $PtSe_2$ /MoSe2 heterostructure. Applied Physics Letters 115, 20 (2019).

[122] Xie, M., Xia, X., Tai, Y., Guo, X., Yang, J., Hu, Y., Xu, L., and Zhang, S. First-principles study on electronic structure and thermodynamic stability of two-dimensional pentagonal M_{X2} (M= Pd, Pt; X= S, Se, Te). Vacuum 212 (2023), 111982.

[123] Xu, H., Huang, H.-P., Fei, H., Feng, J., Fuh, H.-R., Cho, J., Choi, M., Chen, Y., Zhang, L., Chen, D., et al. Strategy for fabricating wafer-scale platinum disulfide. ACS applied materials & interfaces 11, 8 (2019), 8202–8209.

[124] Xu, H., Wei, J., Zhou, H., Feng, J., Xu, T., Du, H., He, C., Huang, Y., Zhang, J., Liu, Y., et al. High spin hall conductivity in large-area type-ii dirac semimetal $PtTe_2$. Advanced Materials 32, 17 (2020), 2000513.

[125] Yang, J., Xie, J., Jiang, S., Zhang, K., Li, Q., Wang, Y., Wang, T., and Su, F. Extraordinary polarization and thickness dependences of photocarrier dynamics in $PdSe_2$ ribbons. The Journal of Physical Chemistry Letters 15, 16 (2024), 4276–4285.

[126] Yao, W., Wang, E., Huang, H., Deng, K., Yan, M., Zhang, K., Miyamoto, K., Okuda, T., Li, L., Wang, Y., et al. Direct observation of spin-layer locking by local rashba effect in monolayer semiconducting $ptse_2$ film. Nature communications 8, 1 (2017), 14216.

[127] Yim, C., Lee, K., McEvoy, N., O'Brien, M., Riazimehr, S., Berner, N. C., Cullen, C. P., Kotakoski, J., Meyer, J. C., Lemme, M. C., et al. High-performance hybrid electronic devices from layered $ptse_2$ films grown at low temperature. ACS nano 10, 10 (2016), 9550–9558.

[128] Yu, J., Kuang, X., Li, J., Zhong, J., Zeng, C., Cao, L., Liu, Z., Zeng, Z., Luo, Z., He, T., et al. Giant nonlinear optical activity in two-dimensional palladium diselenide. Nature communica- tions 12, 1 (2021), 1083.

[129] Yu, J., Zhou, X., Cui, H., Chen, L., Wei, Y., and Tian, T. Ni-dispersed PdS_2 monolayer as a potential sensing material for dissolved gas analysis in electrical transformers: a first-principles study. ACS omega 9, 5 (2024), 5829–5837.

[130] Yu, X., Yu, P., Wu, D., Singh, B., Zeng, Q., Lin, H., Zhou, W., Lin, J., Suenaga, K., Liu, Z., et al. Atomically thin noble metal dichalcogenide: a broadband mid-infrared semiconductor. Nature communications 9, 1 (2018), 1545. 26

[131] Yuan, J., Sun, T., Hu, Z., Yu, W., Ma, W., Zhang, K., Sun, B., Lau, S. P., Bao, Q., Lin, S., et al. Wafer-scale fabrication of two-dimensional pts_2/$ptse_2$ heterojunctions for efficient and broad band photodetection. ACS applied materials & interfaces 10, 47 (2018), 40614–40622.

[132] Yusuf, I. D., Suleiman, A. B., Lawal, A., Ndikilar, C. E., Taura, L., Gidado, A., and Chiromawa, I. M. Significant improvement in structural, electronic, optical and thermoelectric prop- erties of $PdTe_2$ in bulk and monolayer phase: A g0w0+ bse approach. Physica B: Condensed Matter 685 (2024), 416015.

[133] Zeng, L., Han, W., Ren, X., Li, X., Wu, D., Liu, S., Wang, H., Lau, S. P., Tsang, Y. H., Shan, C.-X., et al. Uncooled mid-infrared sensing enabled by chip-integrated low-temperature- grown 2d $pdte_2$ dirac semimetal. Nano Letters 23, 17 (2023), 8241–8248.

[134] Zhang, K. The Growth of Large-Scale Single-Crystal Monolayer Transition Metal Disulfide Materials in High-Vacuum System Based on Passivated Semiconductor. PhD thesis, University of York, 2020.

[135] Zhang, K., Wang, M., Zhou, X., Wang, Y., Shen, S., Deng, K., Peng, H., Li, J., Lai, X., Zhang, L., et al. Growth of large scale ptte, $ptte_2$ and $ptse_2$ films on a wide range of substrates. Nano Research 14, 6 (2021), 1663–1667.

[136] Zhang, K., Yan, M., Zhang, H., Huang, H., Arita, M., Sun, Z., Duan, W., Wu, Y., and Zhou, S. Experimental evidence for type-ii dirac semimetal in $PtSe_2$. Physical Review B 96, 12 (2017), 125102.

[137] Zhang, L., Yang, T., Feng, Y. P., Wee, A. T., Wang, Z., et al. Mbe-grown ultrathin $PtTe_2$ films and their layer-dependent electronic structures. Nanoscale 14, 20 (2022), 7650–7658.

[138] Zhang, L., Yang, T., Sahdan, M. F., Arramel, Xu, W., Xing, K., Feng, Y. P., Zhang, W., Wang, Z., and Wee, A. T. Precise layer-dependent electronic structure of mbe-grown $PtSe_2$. Advanced Electronic Materials 7, 11 (2021), 2100559.

[139] Zhang, M., Yao, N., Lin, Y., Jiang, Z., and Du, A. Spin-orbit coupling induced rashba effect of Cs2 SnBr6 /PdS_2 heterostructure with spin carrier dynamics under pressure. Physical Review B 112, 16 (2025), 165107.

[140] Zhang, S., Ye, Y., Li, H., Kan, X., Wang, S., Sun, S., Han, T., Li, F., Shan, L., and Long, M. High-sensitive ultrabroad photodetector based on $PtSe_2$ /WSe_2 /$PtSe_2$ van der waals heterostruc- ture. Advanced Optical Materials 13, 16 (2025), 2500127.

[141] Zhang, W., Cui, Y., Zhu, C., Huang, B., and Yan, S. Flexible ferroelasticity in monolayer PdS_2 : a dft study. Physical Chemistry Chemical Physics 23, 17 (2021), 10551–10559.

[142] Zhang, X., Su, G., Lu, J., Yang, W., Zhuang, W., Han, K., Wang, X., Wan, Y., Yu, X., and Yang, P. Centimeter-scale few-layer PdS_2 : fabrication and physical properties. ACS applied materials & interfaces 13, 36 (2021), 43063–43074.

[143] Zhang, Y., Tian, H., Li, H., Yoon, C., Nelson, R. A., Li, Z., Watanabe, K., Taniguchi, T., Smirnov, D., Kawakami, R. K., et al. Quantum octets in high mobility pentagonal two- dimensional $PdSe_2$. Nature communications 15, 1 (2024), 761.

[144] Zhao, H., Wang, C., Zhu, Y., Hui, X., and Zhang, L. A density functional theory study on the photocatalytic performance of PtS_2 nanotubes with high carrier mobility for photocatalytic water splitting. Physics Letters A 518 (2024), 129682.

[145] Zhao, W., Cui, C., Xu, Y., Liu, Q., Zhang, Y., Zhang, Z., Lu, S., Rong, Z., Li, X., Fang, Y., et al. Triggering pt active sites in basal plane of van der waals $PtTe_2$ materials by amorphization engineering for hydrogen evolution. Advanced Materials 35, 29 (2023), 2301593. 27

[146] Zhao, W., Ribeiro, R. M., and Eda, G. Electronic structure and optical signatures of semi- conducting transition metal dichalcogenide nanosheets. Accounts of chemical research 48, 1 (2015), 91–99.

[147] Zhao, Y., Qiao, J., Yu, Z., Yu, P., Xu, K., Lau, S. P., Zhou, W., Liu, Z., Wang, X., Ji, W., et al. High-electron-mobility and air-stable 2d layered $ptse_2$ fets. Advanced Materials 29, 5 (2017), 1604230.

[148] Zhao, Y., Yu, P., Zhang, G., Sun, M., Chi, D., Hippalgaonkar, K., Thong, J. T., and Wu, J. Low-symmetry $PdSe_2$ for high performance thermoelectric applications. Advanced Functional Materials 30, 52 (2020), 2004896.

[149] Zhao, Y.-Q., Zhu, L., Zhou, B., and Jiang, S. Chemical vapor deposition of uniform bilayer PtS_2 flakes for electrocatalytic hydrogen evolution. Physical Chemistry Chemical Physics 25, 16 (2023), 11311–11315.

[150] Zheng, H., Choi, Y., Baniasadi, F., Hu, D., Jiao, L., Park, K., and Tao, C. Visualization of point defects in ultrathin layered 1t-$PtSe_2$. 2D Materials 6, 4 (2019), 041005.

[151] Zheng, W., Schönemann, R., Aryal, N., Zhou, Q., Rhodes, D., Chiu, Y.-C., Chen, K.-W., Kampert, E., Förster, T., Martin, T., et al. Detailed study of the fermi surfaces of the type-ii dirac semimetallic candidates XTe_2 (X= Pd, Pt). Physical Review B 97, 23 (2018), 235154.

[152] Zhou, H., Hao, Y., Fan, C., Zhang, S., Wang, C., Wang, K., Zhou, J., Hao, S., Shu, T., Lu, X., et al. Controllable growth of wafer-scale two-dimensional PdS2x Se2(1−x) nanofilms with fully tunable compositions for high-performance photodetectors. Journal of Materials Science & Technology 228 (2025), 200–207.

[153] Zhou, Y., Pan, H., Zhang, Y., Hao, R., Zhu, M., Liu, X., Li, Y., Wang, Z., Wang, X., Zhang, Z., et al. Rayleigh instability triggered growth of 2d horizontal layered and single-phase pts_2 continuous films for high-performance broadband photodetection. Advanced Functional Materials 36, 9 (2026), e10356.

[154] Zhussupbekov, K., Berman, S., Prechtl, M., Busch, M., Zhussupbekova, A., Duesberg, G. S., Nicolosi, V., Novoselov, K. S., Coileáin, C. Ó., and Shvets, I. V. Structural and electronic transition of layered $PtSe_2$ into non-layered PtSe. Nanoscale 17, 9 (2025), 5249–5258.